Check for updates

Green microwave synthesis of pyrazole chalcone molecular hybrids efficient route to advanced diabetes therapeutics with DNA intercalative properties

Jyoti Sharma [ID] and Raj Kaushal [ID] *

Novel chalcone derivatives incorporating pyrazole moieties were synthesized *via* microwave assisted Claisen–Schmidt condensation and evaluated for their *in vitro* α-amylase and α-glucosidase inhibitory potential as therapeutic agents against diabetes mellitus, a rapidly escalating global health crisis. The microwave-assisted approach demonstrated remarkable synthetic advantages achieving excellent yields (80–85%) and enhanced product purity within minutes compared to conventional methods requiring over 24 hours. Five pyrazole-chalcone hybrids, L^I ($C_{19}H_{16}N_2O$), L^{II} ($C_{18}H_{14}Cl_2N_2O$), L^{III} ($C_{18}H_{14}N_3O_3$), L^{IV} ($C_{20}H_{16}N_2O_2$), and L^V ($C_{18}H_{15}N_2O_2$), were successfully synthesized from pyrazole ketone and different substituted aldehydes. Comprehensive structural characterization using FTIR, NMR, UV-Vis, fluorescence, cyclic voltammetry, and mass spectrometry confirmed successful target compound formation. *In vitro* enzyme inhibition studies revealed promising dose dependent activity with compounds L^{IV} ($IC_{50} = 212.5$ μM) and L^{II} ($IC_{50} = 215.2$ μM) demonstrating superior α-glucosidase inhibition compared to acarbose ($IC_{50} = 240.6$ μM), while compound L^I exhibited potent α-amylase inhibitory activity ($IC_{50} = 501.9$ μM). DNA binding studies indicated intercalative interactions with binding constants ranging from 10^3 to 10^4 M^{-1}. Molecular docking analysis revealed stable protein ligand complexes with compound L^{II} showing binding affinities of -6.15 kcal mol^{-1} for α-glucosidase and -5.83 kcal mol^{-1} for α-amylase, while DFT calculations indicated HOMO–LUMO energy gaps of 3.93–4.30 eV suggesting moderate chemical reactivity. The *in silico* drug-likeness and oral bioavailability profiles of pyrazole-chalcone fully comply with Lipinski's criteria and exhibit excellent ADMET properties. These comprehensive findings establish pyrazole chalcone hybrids as promising multifunctional molecular scaffolds with significant potential for next-generation antidiabetic therapeutics.

1. Introduction

Type 2 diabetes mellitus (T2DM) has become a critical global health epidemic of the modern era,[1] impacting approximately 537 million adults worldwide.[2] The condition presents as a multifaceted metabolic disorder distinguished by persistent hyperglycemia,[3] impaired insulin sensitivity, and deteriorating pancreatic β-cell function. The International Diabetes Federation has projected that this number will escalate to 783 million by 2045 underscoring the urgent need for innovative therapeutic interventions.[4] The pathophysiology of T2DM involves intricate dysregulation of glucose homeostasis, with postprandial hyperglycaemia serving as a critical determinant of long-term complications including cardiovascular disease,[5] diabetic nephropathy,[6] retinopathy,[7] and neuropathy.[8,9] Current therapeutic approaches for T2DM management primarily focus on enhancing insulin sensitivity through metformin, stimulating insulin secretion *via* sulfonylureas and glinides, or modulating incretin pathways using GLP-1 receptor[10] agonists[11] and DPP-4 inhibitors.[12] However, these monotherapeutic strategies often prove insufficient in achieving optimal glycaemic control particularly in managing postprandial glucose excursions that significantly contribute to overall glycaemic burden and diabetes related complications. Consequently, there is a compelling need for multitarget therapeutic approaches that can simultaneously address multiple pathophysiological mechanisms underlying T2DM. The digestive enzymes α-amylase and α-glucosidase represent attractive therapeutic targets for postprandial glucose management due to their pivotal roles in carbohydrate metabolism.[13] Pancreatic α-amylase initiates starch digestion by cleaving α-1,4-glycosidic bonds in polysaccharides generating smaller oligosaccharides and maltose units.[14] Subsequently, intestinal α-glucosidase completes the digestive process by hydrolyzing these oligosaccharides and disaccharides into absorbable monosaccharides,

Department of Chemistry, National Institute of Technology, Hamirpur, Himachal Pradesh-177005, India. E-mail: rajkaushal@nith.ac.in

· RSC Advances

primarily glucose, which directly enters systemic circulation.[15] The sequential action of these enzymes makes them ideal targets for controlling postprandial glucose levels as their simultaneous inhibition can effectively delay carbohydrate absorption[16] and mitigate acute hyperglycaemic episodes.[17,18] Acarbose, miglitol, and voglibose represent the current generation of α-glucosidase inhibitors approved for clinical use. While these medications demonstrate efficacy in reducing postprandial glucose levels, they are associated with significant gastrointestinal side effects including flatulence, diarrhoea, and abdominal discomfort, which limit patient compliance and therapeutic effectiveness.[18] Furthermore, these inhibitors primarily target α-glucosidase with limited α-amylase inhibitory activity, potentially missing the opportunity for more comprehensive carbohydrate digestion control.

Chalcones, a class of naturally occurring α, β-unsaturated ketones characterized by the 1,3-diphenyl-2-propen-1-one framework,[19] have garnered substantial attention in medicinal chemistry due to their remarkable structural diversity and broad spectrum of biological activities.[20] Pyrazoles[21] constitute another important class of nitrogen-containing heterocycles with well-established pharmacological significance.[22] The pyrazole core is present in numerous FDA-approved drugs[23] including celecoxib, rimonabant, and sildenafil, highlighting its therapeutic relevance. Pyrazole derivatives exhibit excellent metabolic stability, favourable pharmacokinetic properties, and diverse biological activities[24] including anti-inflammatory,[25] analgesic, antipyretic, and antidiabetic effects.[26,27] The concept of molecular hybridization[28] has emerged as a powerful strategy in modern drug discovery, combining pharmacophoric features from two or more bioactive molecules to create hybrid compounds with enhanced or novel biological properties.[29] Microwave-assisted organic synthesis has revolutionized[30] synthetic chemistry by offering significant advantages[31] over conventional thermal heating methods, enabling rapid and uniform heating, leading to dramatic reductions in reaction times, improved yields, enhanced product purity, and reduced energy consumption.[32]

Despite extensive research on individual chalcone and pyrazole derivatives for antidiabetic applications, systematic investigation of pyrazole-chalcone hybrids as dual α-amylase and α-glucosidase inhibitors remains limited. The present study aims to address these gaps by synthesizing novel pyrazole-chalcone hybrids using microwave-assisted Claisen–Schmidt condensation and evaluating their potential as dual enzyme inhibitors. The comprehensive approach includes detailed structural characterization using multiple analytical techniques, in vitro enzyme inhibition studies, DNA binding investigations, and computational analysis through molecular docking and DFT calculations. The intercalative DNA binding affinity correlates with favourable physicochemical properties for cellular penetration and potential transcriptional modulation of metabolic genes supporting a multitarget antidiabetic mechanism beyond direct enzyme inhibition.[33,34] This multifaceted methodology is designed to provide thorough understanding of structure–activity relationships, binding mechanisms, and molecular properties ultimately contributing

to the development of next-generation antidiabetic therapeutics with improved efficacy and reduced side effects.

2. Experimental section

2.1. Materials

All chemicals and reagents were of analytical grade and used without further purification. Pyrazole-3-carbaldehyde derivatives, acetophenone derivatives, potassium hydroxide, ethanol, and dimethyl sulfoxide (DMSO) were obtained from Sigma-Aldrich. α-Amylase from porcine pancreas (Type VI-B), α-glucosidase from Saccharomyces cerevisiae, 4-nitrophenyl α-D-glucopyranoside (pNPG), starch, and acarbose were purchased from Sigma-Aldrich. Calf thymus DNA (CT-DNA) and ethidium bromide were procured from HiMedia Laboratories.

2.2. Physical methods and analysis

The synthesized compounds were characterized using a comprehensive suite of analytical techniques. Structural elucidation was performed using Fourier Transform Infrared Spectroscopy (FTIR) on a Shimadzu spectrometer in the range of 400–4000 cm^{-1} using the KBr pellet method. Nuclear magnetic resonance (NMR) spectroscopy was conducted on a Bruker Avance NEO 500 MHz spectrometer to obtain both ^{1}H-NMR and ^{13}C-NMR spectra, utilizing DMSO-d$_6$ and CDCl$_3$ as deuterated solvents. Electronic properties were investigated through UV-Vis spectroscopy using a Motras Scientific double-beam spectrophotometer, which also facilitated the evaluation of DNA binding interactions of the synthesized ligands. Fluorescence characteristics were determined using a Shimadzu spectrofluorometer to record emission spectra. Additionally, the electrochemical behaviour of the ligands was examined through cyclic voltammetry studies performed on a Metrohm Autolab three-electrode workstation system.

2.3. Synthesis of 1-(5-methyl-1-phenyl-1H-pyrazol-4-yl)-ethenone

Acetylpyrazole-1 was synthesized following the method described in the literature using phenyl hydrazine 2 (100 mmol), N,N-dimethylformamide-dimethylacetal (DMF-DMA) (17.85 g, 0.15 mol), and acetyl acetone 1 (100 mmol), achieving an 80% yield as shown in Scheme 1 FTIR spectrum: (KBr, ū cm^{-1}) 3060, 3001, 2936, 1660, 1657, 1545, 1502, 1457, 1400, 1383, 1276, 1239, 1197, 938, 770, 700, 689, 659. ^{1}H-NMR: (500 MHz, CDCl$_3$): δ(ppm) 8.00 (s, 1H, Pyrazole-H), 7.51–7.40(m, 5H, Ar–H), 2.57 (s, 3H, COCH$_3$), 2.48 (s, 3H, CH$_3$). ^{13}C-NMR: (500 MHz, CDCl$_3$) 193 (CO), 138, 129, 128, 125 (aromatic ring C atoms), 28.83, 12.36 (two CH$_3$), 143.17, 142.23, 121.26 (pyrazole ring C atoms). ESI: (m/z %): found 201.09 (M + H), exact mass 200, 223.08 (M + Na).

2.4. Preparation of pyrazole chalcones

2.4.1. Conventional method. A solution of pyrazole ketone in ethanol/methanol was added to a solution of various aldehydes in ethanol/methanol in a 1 : 1 ratio. To this mixture, 3 M NaOH solution was added dropwise, and the reaction was
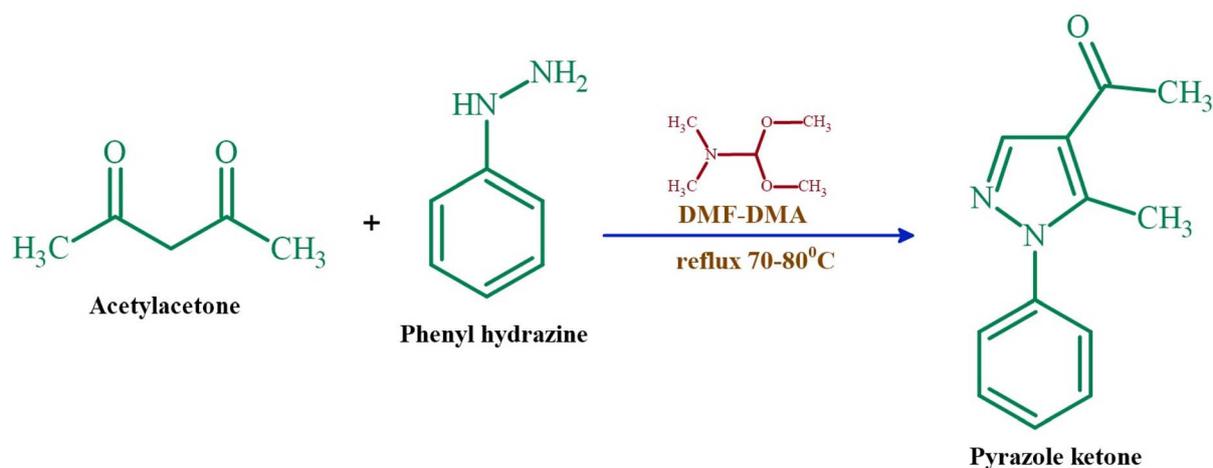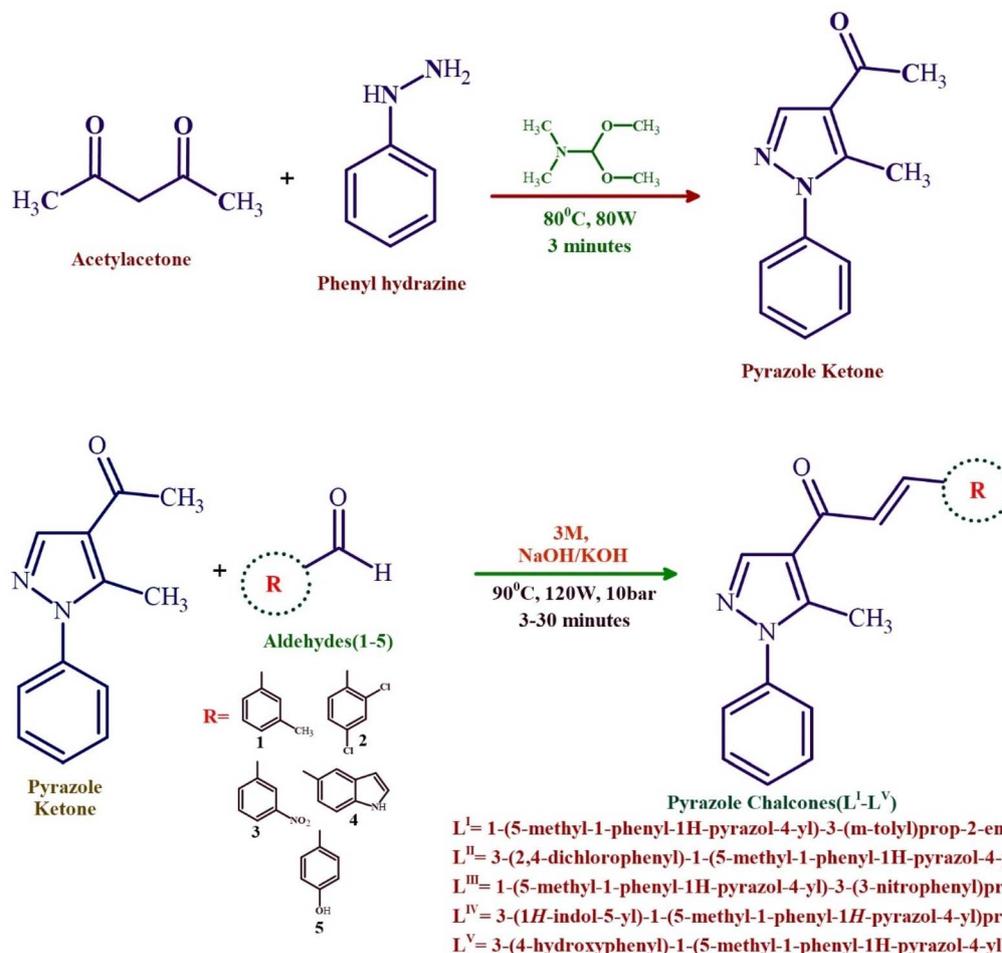
Scheme 1 Synthesis of pyrazole ketone.

sonicated for 4–5 hours. The progress of the reaction was monitored using TLC. After the reaction was complete, the mixture was neutralized using 2 M HCl and the resulting precipitate was filtered and dried. General procedure for chalcone synthesis is as shown below in Scheme 2.[35]
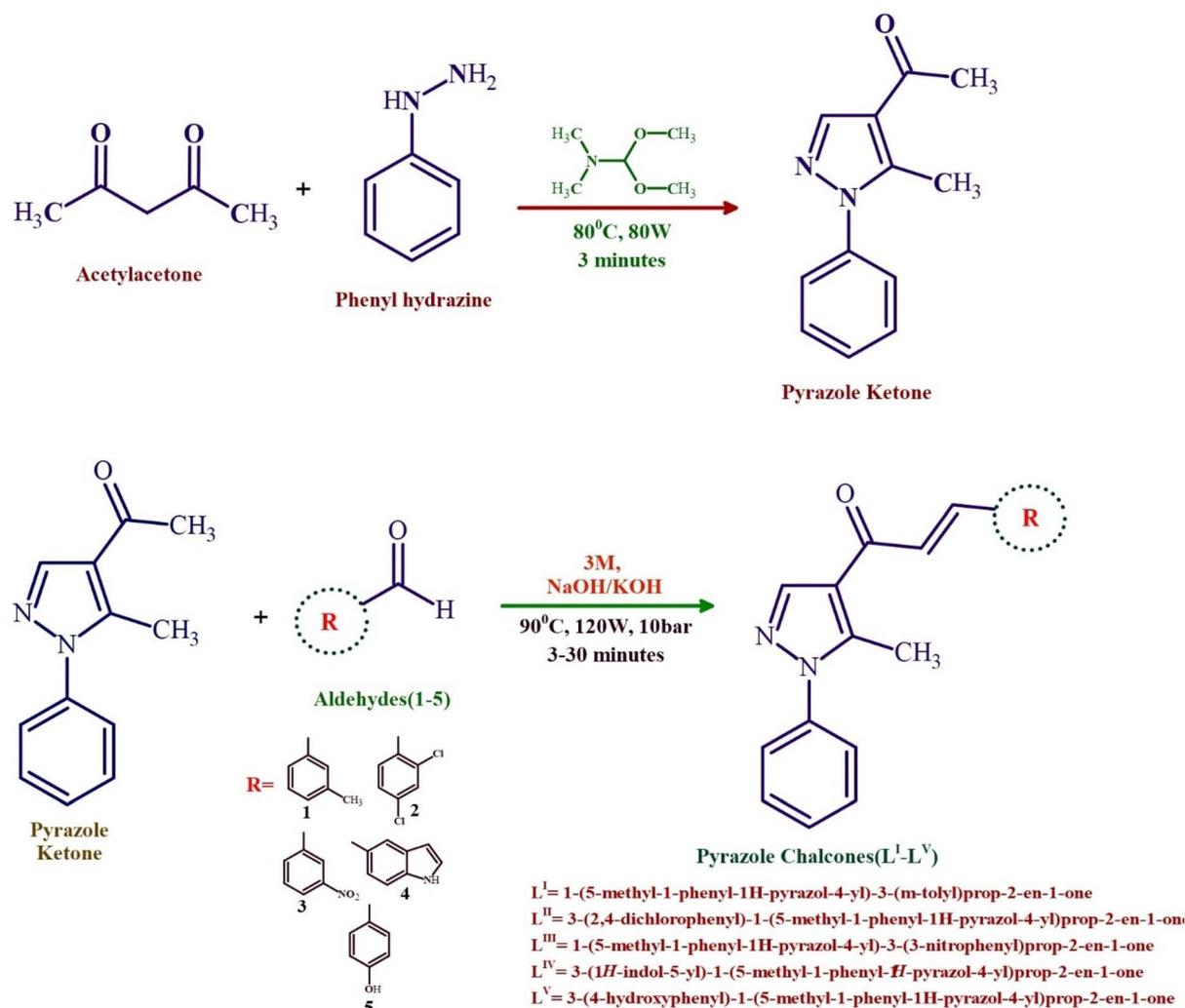
2.5. Microwave assisted synthesis of pyrazole chalcones

Pyrazole chalcones were obtained by subjecting methyl ketones and aromatic aldehydes to Claisen–Schmidt condensation under microwave irradiation (see Scheme 3 and Table 3). The reactions went successfully with good to outstanding yields (70–

L^{I} = 1-(5-methyl-1-phenyl-1H-pyrazol-4-yl)-3-(m-tolyl)prop-2-en-1-one

L^{II} = 3-(2,4-dichlorophenyl)-1-(5-methyl-1-phenyl-1H-pyrazol-4-yl)prop-2-en-1-one

L^{III} = 1-(5-methyl-1-phenyl-1H-pyrazol-4-yl)-3-(3-nitrophenyl)prop-2-en-1-one

L^{IV} = 3-(1H-indol-5-yl)-1-(5-methyl-1-phenyl-1H-pyrazol-4-yl)prop-2-en-1-one

L^{V} = 3-(4-hydroxyphenyl)-1-(5-methyl-1-phenyl-1H-pyrazol-4-yl)prop-2-en-1-one

Scheme 2 Synthesis of pyrazole chalcones by Claisen Schmidt condensation by conventional method.

Scheme 3 Microwave assisted synthesis of pyrazole ketone and its chalcone derivatives.

98%). Taking into consideration a green approach, a reduction in the longer reaction time, and minimising the excess usage of base, hence producing less chemical waste, the reaction was reconfigured to be conducted under microwave irradiation. In a microwave reaction vessel (10 mL), 2 equivalents of KOH/NaOH were added to a solution of pyrazole ketone and

Table 1 Comparative analysis of reaction times and product yields for chalcone derivatives using conventional and microwave synthetic approaches

Ligand	Conventional method			Microwave method	
	Time	Condition	Yield	Time	Yield
Pyrazole ketone	24 h	80 °C reflux	70%	3 minutes	90%
L^I	24 h	45–50 °C stirring	72%	10 minutes	85%
L^{II}	>24 h	RT stirring	75%	3 minutes	85%
L^{III}	24 h	50–55 °C stirring	55%	13 minutes	80%
L^{IV}	>24 h	50–55 °C stirring	60%	35 minutes	85%
L^V	24 h	45–50 °C stirring	55%	20 minutes	80%

different aldehydes dissolved in methanol/ethanol (7 mL). The resultant combination was then irradiated for different time intervals in a CEM microwave synthesiser with 120 W, 90 °C, and an internal pressure of 10 bar. After completing the reaction, the reaction vessel was cooled down to room temperature, and then corresponding precipitates began to separate out.[36]

The compounds synthesized using the microwave method are obtained in a highly pure form, as evidenced by a single, clear spot on the TLC, unlike those from the conventional method, which show multiple side products. Additionally, the microwave method results in a higher yield of the final product. The comparative analysis of the both methods is shown in Table1.

2.5.1. 1-(5-methyl-1-phenyl-1H-pyrazol-4-yl)-3-(m-tolyl) prop-2-en-1-one (L^I). Yield: 85.02%, FTIR spectrum: (KBr, ū cm^{-1}) 3066, 2909, 2355, 1650, 1591, 1539, 1500, 1452, 1397, 1307, 1272, 1227, 1182, 989, 940, 851, 791, 762, 692, 583, 509. ^{1}H-NMR: (500 MHz, CDCl$_3$): δ(ppm) 8.16 (s, 1H, Pyrazole-**H**), 7.78 (d, 1H, –C=C**H**), 7.23 (d, 1H, CO**CH**), 7.54–7.30 (m, 9H, Ar–**H**), 2.66 (s, 3H, pyrazole C**H$_3$**), 2.41 (s, 3H, C**H$_3$**). ^{13}C-NMR: (500 MHz, CDCl$_3$) 185 (CO), 143 (C=CH), 121 (COCH), 134, 131, 125,

123 (aromatic ring C atoms), 144, 141, 21 (pyrazole C atoms), 138, 129, 128 (phenyl C atoms). ESI: (m/z %): found 303.14 (M + H), exact mass 302.

2.5.2. 3-(2,4-dichlorophenyl)-1-(5-methyl-1-phenyl-1H-pyrazol-4-yl)prop-2-en-1-one (L^{II}). Yield: 80.1%, FTIR spectrum: (KBr, ū cm^{-1}) 3076, 3066, 1662, 1605, 1581, 1547, 1504, 1470, 1453, 1391, 1308, 1269, 1214, 1184, 1151, 1100, 1045, 1006, 967, 940, 906, 881, 851, 821, 751, 723, 688, 658. ^{1}H-NMR: (500 MHz, CDCl$_3$): δ(ppm) 8.1 (s, 1H, Pyrazole-H), 8.0 (d, 1H, −C=CH), 7.7 (d, 1H, COCH), 7.5 (m, 2H, Ar–H), 7.4 (m, 4H, Phenyl-H), 2.6 (s, 3H, CH$_3$). ^{13}C-NMR: (500 MHz, CDCl$_3$) 184 (CO), 144 (C=CH), 138, 137, 136, 131, 130, 129, 128, 127, 126, 125 (aromatic ring C atoms), 121 (COCH). ESI: (m/z %): found: 411.09 (M + Na), exact mass 357.

2.5.3. 1-(5-methyl-1-phenyl-1H-pyrazol-4-yl)-3-(3-nitrophenyl) prop-2-en-1-one (L^{III}). Yield: 82%, FTIR spectrum: (KBr, ū cm^{-1}) 3076, 2869, 1658, 1609, 1528, 1347, 998, 1284, 1216, 1189, 1096, 1069, 997, 938, 852, 814, 766, 745, 724, 695. ^{1}H-NMR: (500 MHz, CDCl$_3$): δ(ppm) 8.5 (s, 1H, pyrazole-H), 8.2, 8.1(m, 2H, Ar–H), 7.9(s, 1H, C=CH), 7.8(d, 1H, COCH), 7.6, 7.5(m, 2H, Ar–H) 7.4(m, 3H, phenyl-H), 2.6(s, 1H, CH$_3$). ^{13}C-NMR: (500 MHz, CDCl$_3$) 185(CO), 144(pyrazole-C atom), 121(COCH), 141(C=CH), 138, 134, 131, 129, 128, 125(aromatic C atoms). ESI: (m/z %): found 334 (M + H), exact mass 333.

2.5.4. 3-(1H-indol-5-yl)-1-(5-methyl-1-phenyl-1H-pyrazol-4-yl) prop-2-en-1-one (L^{IV}). Yield: 79.23%, FTIR spectrum: (KBr, ū cm^{-1}) 3059, 3032, 1648, 1568, 1540, 1505, 1472, 1454, 1403, 1351, 1284, 1221, 1182, 1131, 1095, 1019, 1006, 943, 896, 863. ^{1}H-NMR: (500 MHz, CDCl$_3$): δ(ppm) 11.3(s, 1H, NH), 8.6(s, 1H, pyrazole-H), 8.0(s, 1H, Ar–H), 7.7(d, 1H, C=CH), 7.4(d, 1H, COCH), 7.6, 7.5, 7.4(m, 7H, Ar–H), 2.5(s, 1H, CH$_3$). ^{13}C-NMR: (500 MHz, CDCl$_3$) 184(CO), 144(pyrazole-C atom), 141(C=CH), 137, 136, 131, 129, 128, 127, 126, 121(aromatic C atoms). ESI: (m/z %): found 335 (M + Li + H), exact mass 327.

2.5.5. 3-(4-hydroxyphenyl)-1-(5-methyl-1-phenyl-1H-pyrazol-4-yl)prop-2-en-1-one (L^V). Yield: 78.1%, FTIR spectrum: (KBr, ū cm^{-1}) 3305, 3010, 2932, 2861, 1630, 1586, 1518, 1457, 1367, 1342, 1298, 1245, 1218, 1166, 1038, 959, 898, 795, 732, 678, 595, 535. ^{1}H-NMR: (500 MHz, CDCl$_3$): δ(ppm) 8.1(s, 1H pyrazole-H), 7.7(d, 1H, C=CH), 7.5–7.3(m, 7H, Ar–H), 6.8(d, 1H, COCH), 2.5(s, 3H, CH$_3$). ESI: (m/z %): found 343 (M + K), exact mass 304.

2.6. Enzyme inhibition studies

2.6.1. *In vitro* α-amylase inhibitory assay. The α-amylase inhibitory activity was evaluated *in vitro* using the iodine-starch method. The method was adapted with slight modifications from the studies of M. Kaur and R. Kaushal.[37] The experimental setup involved three key components to evaluate α-amylase inhibition. A blank solution (B) containing starch without α-amylase produced a characteristic intense blue coloration upon iodine addition. The control solution (C) included α-amylase but lacked any inhibitory compounds, resulting in an almost colourless appearance due to complete starch hydrolysis. When pyrazole chalcones were introduced, blue coloration reappeared with iodine-starch complex formation, demonstrating partial

enzyme inhibition at various levels. The inhibition assay was conducted by preparing serial dilutions of the synthesized compounds and acarbose (positive control) in reaction buffer (10 mM sodium phosphate buffer, pH 6.9, with 6 mM sodium chloride). These solutions were pre-incubated with α-amylase (20 units per mL, 100 μL) for 30 minutes at 37 °C. Following pre-incubation, 100 μL of 1% starch substrate was introduced, and the mixture was incubated for an additional 20 minutes at 37 °C. The enzymatic reaction was stopped by adding 100 μL of hydrochloric acid. Colour development was initiated by incorporating 200 μL of iodine solution, after which the mixture was diluted with 1 mL of deionized water. Spectrophotometric analysis was performed at 620 nm to quantify the blue colour intensity.[38] After subtracting the blank absorbance (enzyme and starch-free sample), the percentage of α-amylase inhibition was determined using the formula:

$$\% \text{ inhibition} = \frac{\text{As} - \text{Ab}}{\text{Ac} - \text{Ab}} \times 100$$

where As = absorbance of the test sample, Ab = absorbance of the blank (excluding test sample and starch) and Ac = absorbance of the control (excluding test sample and α-amylase)

2.6.2. *In vitro* α-glucosidase inhibitory assay. The α-glucosidase inhibitory potential was evaluated following established literature protocols with minor adaptations,. The assay employed varying concentrations of the synthesized test compounds to determine their inhibitory effects. The experimental procedure involved preparing reaction mixtures containing different sample dilutions in phosphate buffer (10 mM; pH 6.9), which were pre-incubated at 37 °C for 20 minutes alongside 20 μL of yeast α-glucosidase enzyme (5 units per mL). Following the pre-incubation period, 200 μL of 1 mM p-Nitrophenyl-β-D-Glucopyranoside (pNPG) substrate was introduced to initiate the enzymatic reaction. The extent of enzyme inhibition was determined by spectrophotometric measurement at 405 nm after diluting the reaction mixture with 1 mL of deionized water. The obtained absorbance values were benchmarked against acarbose, which served as the standard reference control.[39] The percentage inhibition of α-glucosidase activity was subsequently computed using the established calculation formula:

$$\% \text{ inhibition} = 1 - \frac{\text{Abs}_{\text{(sample)}}}{\text{Abs}_{\text{(blank)}}} \times 100$$

2.6.3. Kinetic studies of enzyme inhibition. Kinetic studies were conducted to determine the inhibition mechanism of pyrazole engrafted chalcones against α-glucosidase and α-amylase.[40] Reactions were set up using varying concentrations of substrates p-NPG for α-glucosidase and starch for α-amylase while keeping enzyme concentrations constant (5 U ml^{-1} for α-glucosidase and 20 U ml^{-1} for α-amylase), along with a fixed inhibitor concentration (50 μM) based on the best IC$_{50}$ value. Control experiments without the inhibitor were also carried out. Reaction velocities were measured over time, and data were interpreted using Michaelis–Menten and Lineweaver-Burk plots

to assess changes in V_{max} and K_m, thereby identifying the type of enzyme inhibition involved.

$$\frac{1}{V} = \frac{K_m}{V_{max}[S]} + \frac{1}{V_{max}}$$

2.7. DNA binding studies

The interactions of the synthesized compounds with calf-thymus DNA were investigated using a variety of spectroscopic techniques such as absorption spectroscopy, emission spectroscopy and cyclic voltammetry.

2.7.1. Absorption spectroscopy. Absorption spectrum titrations were performed in phosphate buffer (0.01 M, pH 7.2) at room temperature spanning the wavelength range of 200–500 nm. Two sets of experiments were conducted: (i) keeping the ligand concentration fixed (50 μM) and progressively increasing the DNA concentration (0–80 μM) and (ii) keeping the DNA concentration constant at 25 μM and altering the ligand concentration from 1–50 μM. The concentration of ct-DNA in stock solutions was calculated from its absorbance at 260 nm using a molar extinction coefficient ($\varepsilon 260 = 6600$ L mol^{-1} cm^{-1}). To reduce the background contribution of DNA, identical amounts of DNA solution were applied to both the reference and test cuvettes before measuring.

2.7.2. Emission spectroscopy. Fluorescence experiments were performed on a Shimadzu RF-5000 spectrofluorometer with 10 nm excitation and emission slits. Emission spectra were recorded in the 270–500 nm range, with excitation wavelengths chosen based on the absorption maxima of each molecule. All intensities were represented as arbitrary units (a.u). Two types of titrations were performed in phosphate buffer (0.01M, pH 7.2) at room temperature: (i) in the ethidium bromide (EB) displacement assay, a preformed EB-DNA complex was titrated with varying ligand concentrations to monitor fluorescence quenching and competitive binding and (ii) in ligand DNA interaction studies, a fixed concentration of ct-DNA (25 μM) was titrated with increasing concentrations of each ligand (1–50 μM). To guarantee homogeneity, both solutions were gently mixed before spectral capture.

2.7.3. Electrochemical studies. The electrochemical measurements were conducted using a three-electrode cell setup, consisting of a glassy carbon working electrode, a platinum wire auxiliary electrode, and Ag/AgCl as reference electrode, all housed in a single compartment. Before each experiment, the glassy carbon electrode was polished with alumina powder. The cyclic voltammetry measurements for compound were performed in phosphate buffer (pH 7.2) as the supporting electrolyte, both with and without DNA present. All measurements were conducted at room temperature, scanning between +2.0 and −2.0 V at a rate of 50 mV s^{-1}.

2.8. Computational studies

2.8.1. Molecular docking studies. Molecular docking simulations were carried out to assess the binding modes and interactions of the compounds within the active sites of α-amylase and α-glucosidase. The flare software suite was utilized to conduct molecular docking (MD) studies on all the synthesized compounds. The 3D structures of all the derivatives were generated using the Chem Draw/Chemsketch software. The structural coordinates for both α-amylase and α-glucosidase were retrieved from the Protein Data Bank (https://www.rcsb.org) using PDB codes 3VX0 and 3W37, respectively. The docking process for all the compounds was carried out by positioning them within the active sites of each protein, guided by the co-crystal residues present in these sites. This was performed using the normal docking module, employing its default molecular docking parameters to ensure accurate simulation of the binding interactions. The docked complexes were subsequently evaluated and ranked based on their protein-ligand interaction (PLI) profiles.

2.8.2. *In silico* pharmacokinetics ADMET prediction and drug likeness prediction. *In silico* prediction of pharmacokinetic parameters (ADMET: absorption, distribution, metabolism, excretion, and toxicity) and drug-likeness properties of the selected compounds was carried out using two widely recognized web-based tools pkCSM (http://biosig.unimelb.edu.au/pkcsm/) and SwissADME (http://www.swissadme.ch/). pkCSM was employed to evaluate key pharmacokinetic and toxicity parameters including intestinal absorption, blood–brain barrier permeability, cytochrome P450 interactions, clearance, and potential toxicity risks. SwissADME was utilized to predict drug-likeness, physicochemical descriptors, lipophilicity, solubility, pharmacokinetics, and medicinal chemistry friendliness. In addition, Lipinski's rule of five, Veber's rule, and Muegge's criteria were applied through SwissADME to assess oral bioavailability. The predicted values provided a comprehensive understanding of the pharmacokinetic behaviour and drug-likeness profile of the compounds facilitating their evaluation as potential drug candidates.

2.8.3. Density functional theory studies. The molecular structures of all synthesized compounds were constructed using the Spartan '24 software. Initial geometry optimizations were performed to obtain suitable starting structures. The optimized geometries were then subjected to quantum mechanical calculations. DFT studies were carried out to explore the electronic properties, molecular orbitals, and reactivity of the synthesized compounds. The hybrid B3LYP functional paired with the 6-31G* basis set was chosen for calculations based on its proven balance of accuracy and computational tractability. Complete structural optimizations were conducted under gas-phase conditions to locate the lowest energy conformations for each molecule.

2.8.3.1. Molecular orbital analysis. The frontier molecular orbitals (FMOs), specifically the highest occupied molecular orbital (HOMO) and the lowest unoccupied molecular orbital (LUMO), were analysed to assess the compounds' electronic properties. The HOMO–LUMO energy gap (ΔE) was calculated to provide insights into the stability and reactivity of the molecules. Additionally, molecular electrostatic potential (MEP) surfaces were generated to visualize the charge distribution and potential interaction sites.

2.8.3.2. Global reactivity descriptors. Global reactivity descriptors such as ionization potential (IP), electron affinity (EA), chemical hardness (η), chemical potential (μ), global

electrophilicity index (ω), chemical softness (S), and absolute electronegativity (χ) were derived from the HOMO and LUMO energies using Koopmans' approximation:

$$\text{Energy Gap } (\Delta E) = E(\text{LUMO}) - E(\text{HOMO})$$

$$\text{Ionization Potential } (P) = -E(\text{HOMO})$$

$$\text{Electron Affinity } (A) = -E(\text{LUMO})$$

$$\text{Chemical potential}(\mu) = \frac{E(\text{HOMO}) + E(\text{LUMO})}{2}$$

$$\text{Chemical hardness}(\eta) = \frac{E(\text{LUMO}) - E(\text{HOMO})}{2}$$

$$\text{Electrophilicity index}(\omega) = \frac{\mu^2}{2\eta}$$

$$\text{Chemical softness}(S) = \frac{1}{\eta}$$

$$\text{Absolute electronegativity } (\chi) = -\mu$$

3. Result and discussion

3.1. FTIR analysis

The IR spectrum of the pyrazole ketone shows several characteristic absorption bands that confirm its structural features.[41] The main absorption peaks can be observed at: 3280–2934 cm^{-1} (a broad band arising from C–H stretching vibrations of both aliphatic and aromatic groups), 1660 cm^{-1} (a strong, sharp peak characteristic of C=O stretching vibration indicating the presence of a ketone group), 1578 cm^{-1} (corresponding to C=N stretching of the pyrazole ring), 1458 cm^{-1} (attributed to C=C stretching vibrations of the aromatic ring system), and 1276 cm^{-1} (representing C–N stretching vibration that further confirms the pyrazole heterocycle). The positions and intensities of these absorption bands providing strong evidence for the presence of all key functional groups including the carbonyl group, aromatic ring system, pyrazole heterocycle, and various C–H bonds. The IR spectrum of pyrazole chalcone compounds exhibits several distinctive absorption bands that confirm its structural features. The major peaks appear at: 2919 cm^{-1} (corresponding to stretching vibrations of the CH$_3$ group), 1656 cm^{-1} (indicating C=O stretching of the carbonyl group), 1607 cm^{-1} (representing C=C stretching of the aromatic ring), and 1541 cm^{-1} (attributable to C=C/C=N stretching of the pyrazole ring). Additionally, peaks at 1254 and 1434 cm^{-1} correspond to C–N stretching vibrations. The carbonyl (C=O) stretching frequency decreases from 1660 cm^{-1} in the pyrazole core to 1656–1640 cm^{-1} in the ligand occurs because the carbonyl group becomes conjugated with the neighbouring C=C bond. The formation of the ligand is confirmed by two key spectral features: the shift in the carbonyl (C=O) stretching frequency and the appearance of C=C stretching bands in the 1500–1600 cm^{-1} region. These characteristic changes in the IR spectrum serve as definitive evidence for successful ligand formation.[42] The significant vibrational frequencies are compiled in Table 2 with the respective FTIR spectra illustrated in Fig. S1–S6.

3.2. NMR spectroscopy

^{1}H-NMR data: The ^{1}H NMR spectrum of the pyrazole nucleus shows a singlet at δ 8.05 ppm corresponding to the pyrazole ring proton, while the phenyl ring protons appear as a multiplet pattern in the range of δ 7.40–7.60 ppm. In the aliphatic region, two distinct signals at δ 2.60 ppm and 2.40 ppm are observed for the methylene protons. The ^{1}H NMR spectra of the chalcones, recorded in CDCl$_3$, showed distinct and well-resolved signals. The α, β-unsaturated protons appeared as doublets in the range of 7.2–8.0 ppm, while all compounds (L^I–L^V) showed

Table 2 Vibrational frequencies of ligands (L^I–L^V)

Ligands	Vibrational frequencies (cm^{-1})
Pyrazole ketone	3060–2934 (CH$_3$str), 1660 (C=O), 1596 (C=C pyrazole ring), 1545–1505 (C=C phenyl ring), 1458 (C=N), 1275 (C–N)
L^I	3052, 3033 (CH$_3$ str), 2914, 2851 (CH$_3$ str), 1650 (C=O), 1597 (C=C enone), 1541–1503 (C=C aromatic), 1453 (C=N), 1269 (C–N)
L^{II}	3078–3066 (CH3 str), 1662 (C=O), 1605 (C=C enone), 1547 (C=N), 1392 (C–N), 550–880 (C–Cl)
L^{III}	3071, 3024 (CH$_3$ str), 2866 (C=CH str), 1659 (C=O), 1610 (C=C enone), 1523 (NO2 asy atr), 1502–1453 (C=C aromatic), 1380 (NO$_2$ *sym* str), 1352 (C=N), 1284 (C–N), 997 (NO$_2$ scr)
L^{IV}	3229 (N–H), 3057,3024 (CH$_3$ str), 1645 (C=O), 1568 (C=C enone), 1540 (N–H bend), 1504 (C=C phenyl ring), 1455 (C=N), 1284 (C–N), 1007 (N–H wag)
L^V	3305 (O–Hs str), 3010 (CH$_3$ str), 2861 (C=CH), 1630 (C=O), 1568 (C=C enone), 1515 (C=C aromatic), 1452 (C=N), 1245 (C–N)

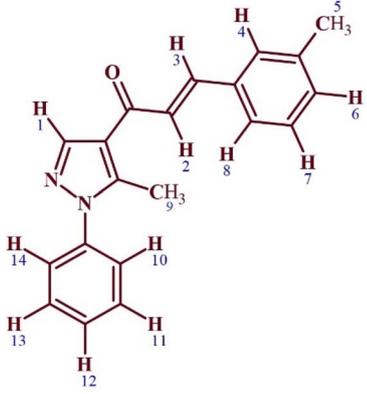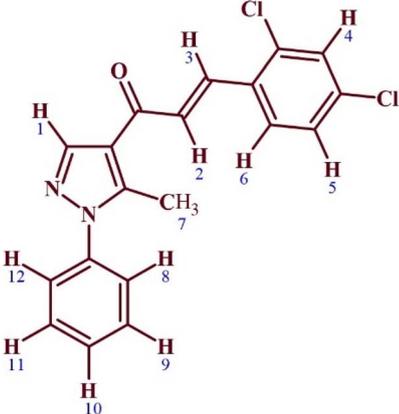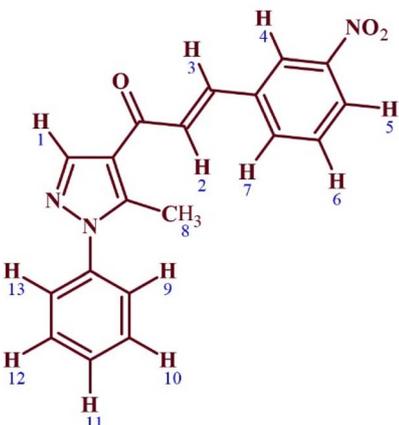**Table 3** The ^{1}H-NMR shifts of pyrazole ketone and ligands (L^I–L^{II})

Ligands	^{1}H-NMR signals (ppm)
	8.0 (H1), 7.51–7.40 (H4–H8), 2.48 (H2), 2.57 (H3)
	8.16 (H1), 7.75 (H3), 7.23 (H2), 7.32 (H4, H6), 7.45–7.54 (H7, H8, H10–H14), 2.66 (H9), 2.41 (H5)
	8.14 (H1), 8.08 (H3), 7.69 (H2), 7.45–7.55 (H5, H6, H8, H9, H11, H12), 7.30–7.32 (H10, H4), 2.66 (H7)
	8.51 (H1), 8.2 (H5), 8.1 (H4), 7.9 (H3), 7.8 (H2), 7.6 (H7), 7.5 (H6), 7.4 (H9– H13), 2.6 (H8)

Table 3 (Contd.)
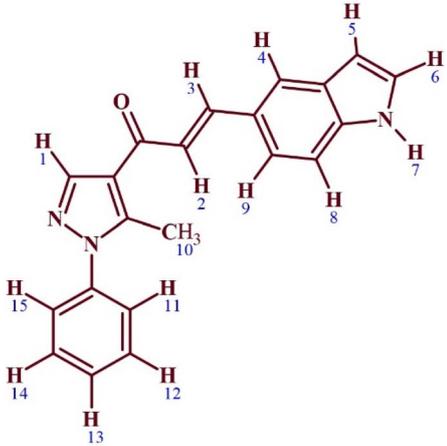
| Ligands	^{1}H-NMR signals (ppm)
	9.9 (H7), 8.2 (H4), 8.19 (H1), 7.9 (H3), 7.45 (H2), 7.47 (H11–H15), 7.51 (H8, H9), 7.52 (H6), 6.62 (H5), 2.67 (H10)
	9.8 (H6), 8.04 (H1), 7.7 (H3, H4), 7.39–7.52 (H10–H14, H8), 6.91 (H2, H5, H7), 2.57 (H9)
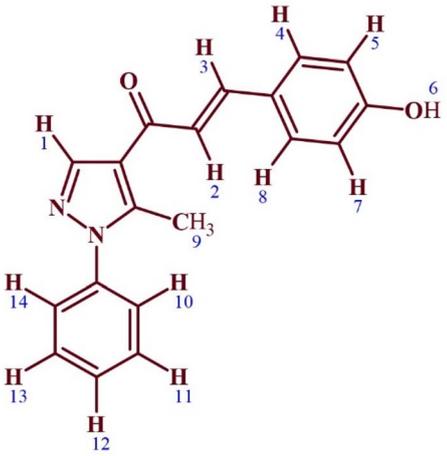
a characteristic singlet at 2.31 ppm corresponding to methyl protons. All aromatic protons were observed in the range of 6.0–8.0 ppm.[43] The characteristic proton NMR peaks for all ligands are summarized in Table 3 while the corresponding ^{1}H-NMR spectra are presented in Fig. S7–S12.

3.2.1. ^{13}C-NMR data. The ^{13}C NMR spectra of all synthesised compounds showed well-defined resonance signals corresponding to the predicted carbon environments, indicating structural integrity. A unique carbonyl resonance for the pyrazole ketone moiety was detected at around 193 ppm, which moved to 183–184 ppm in the chalcone derivatives, indicating successful inclusion of the chalcone framework. Furthermore, aromatic carbon signals appeared in the predicted 150–120 ppm range, indicating the presence of aromatic rings within the structures. Overall, the ^{13}C NMR findings give solid support for the effective synthesis of the desired pyrazole chalcones.[44] The ^{13}C-NMR spectra of all synthesized ligands are presented in Fig. S13–S16.

3.3. Mass spectrometry

The mass spectral analysis of the ligands provided additional confirmation of the successful formation of the desired ligands. The pyrazole ketone exhibits a protonated molecular ion (M + H) at m/z 201 (calc. M = 200), while $\mathbf{L^{III}}$ shows a protonated peak at m/z 334 (calc. M = 333), indicating straightforward protonation under ESI conditions. Several additional ligands produced peaks at higher m/z than the calculated neutral mass; such shifts are frequent in ESI and can be easily explained by adduct formation (alkali-metal adducts, solvent or counter-ion addition) or mild aggregation. For example, the peaks detected at m/z 341 ($\mathbf{L^{I}}$, calc. 302), m/z 343 ($\mathbf{L^{V}}$, calc. 304) and m/z at 335 ($\mathbf{L^{IV}}$, calc. 327) are compatible with the addition of a potassium ion and lithium ion ([M + K]/[M + Li]) or similar alkali-metal adducts. Other shifted peaks likely come from solvent/counter-ion adducts or in-source clustering. The general fragmentation pattern for the chalcone derivatives is shown in Scheme 4. The mass spectra of all synthesized ligands are presented in Fig. S17–S22.
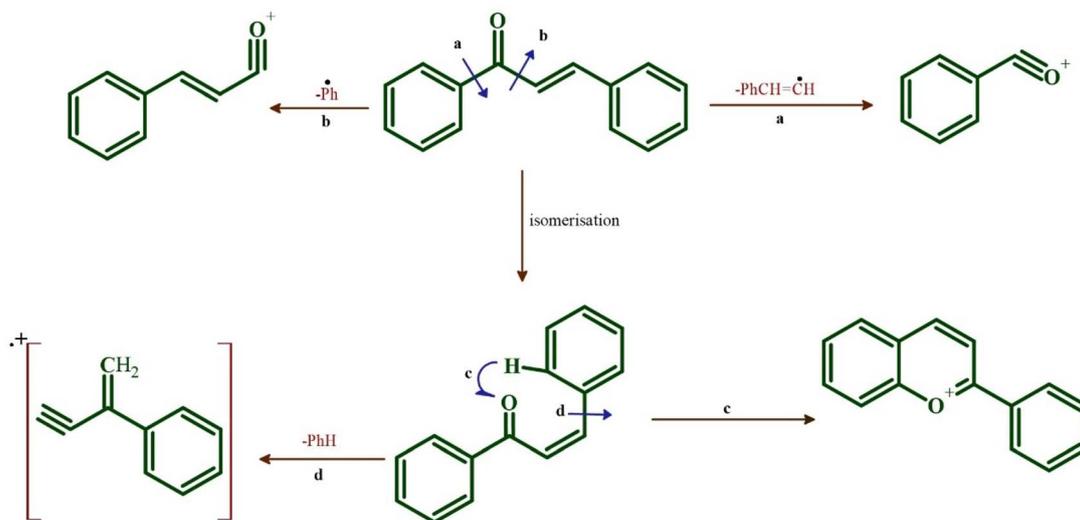
Scheme 4 Generalized fragmentation mechanisms of chalcone derivatives yielding daughter ion species.

3.4. Enzyme inhibition studies

Throughout the bio-assay technique all compounds demonstrated acceptable stability under physiological circumstances (pH 7.4, 37 °C) with no apparent precipitation or activity loss demonstrating their eligibility for biological evaluation.

3.4.1. Determination of α-glucosidase inhibition. *In vitro* assays were conducted to evaluate the α-glucosidase inhibitory effects of pyrazole-chalcone hybrids (L^I–L^V), using acarbose as a reference standard. All the ligands exhibited a dose-dependent inhibition pattern, as evidenced by an increase in % inhibition with rising inhibitor concentrations. The α-glucosidase inhibition study revealed that $L\square$ (IC_{50} = 212.5 μM) and $L\square\square$ (IC_{50} = 215.2 μM) exhibited the most potent activity, surpassing the standard drug acarbose (IC_{50} = 240.6 μM). The strong inhibition by $L\square$ is likely due to the indole ring, which enhances π–π stacking and hydrophobic interactions, while $L\square\square$ benefits from dichloro substituents that promote strong electron-withdrawing effects and better enzyme binding. Moderate inhibition was observed for $L\square\square\square$ (IC_{50} = 281.1 μM), while $L\square$ (393.6 μM) and L^V (373.6 μM) showed weaker activity, possibly due to limited binding affinity or solubility issues. These results highlight the importance of substituent type and position in influencing enzyme interaction and inhibition.[45] The inhibition results are shown in Table 4.

3.4.2. Determination of α-amylase inhibition. A summary of α-amylase inhibition outcomes is provided in Table 5. The inhibition data revealed that all compounds displayed dose-dependent enzyme inhibition, as reflected by the increasing % inhibition with rising concentrations. Among the series, compound $L\square$ (derived from *m*-tolualdehyde) showed the most potent inhibitory activity with an IC_{50} value of 501.93 μM, significantly better than the rest of the ligands but still less active than the standard drug acarbose (IC_{50} = 301.9 μM). The enhanced activity of $L\square$ may be attributed to the meta-methyl group, which likely improves hydrophobic interactions within the enzyme's active site, facilitating stronger binding. In

contrast, compounds $L\square\square$ to L^V demonstrated significantly lower inhibitory effects. Notably, $L\square\square\square$ (bearing an electron-withdrawing nitro group) and $L\square$ (containing a bulky indole moiety) showed the weakest inhibition, with IC_{50} values of 984.4 μM and 2416.0 μM, respectively—possibly due to steric hindrance or poor electronic complementarity with the active site. The 4-hydroxybenzaldehyde-based ligand L^V showed moderate inhibition (IC_{50} = 1618 μM), which may stem from limited binding interactions or solubility constraints affecting enzyme access.[46] The inhibition results are shown in Table 5.

3.4.3. Kinetic studies of enzyme inhibitions. Inhibitors can target enzymes in many ways to prevent their action during metabolism. The Lineweaver–Burk plot was used to determine the inhibition mechanism of the enzyme by complex inhibitors. The double reciprocal plot of 1/[S] v/s 1/[V] reveals a linear relationship between substrate concentration [S] and reaction velocity. The graph shows that the ordinate intercept equals $1/V_{max}$, while the negative abssica intercept equals $[-1/K_m]$. The kinetic parameters calculated are listed in Table 6 below. Although both V_{max} and K_m decreased for α-glucosidase in the presence of the inhibitor (shown in Fig. 1), numerically suggesting uncompetitive inhibition, the Lineweaver–Burk plot displays intersecting lines in the second quadrant shown in

Table 4 α-glucosidase inhibitory activity of ligands L^I–L^V and their IC_{50} value

| Ligand | %Inhibition at each concentration (μM) | | | | | | | IC_{50} (μM) |
	10	40	100	140	350	400	500	
L^I	9.43	11.83	16.05	17.53	37.07	47.52	71.09	393.61
L^{II}	17.74	16.81	26.96	33.37	78.29	89.86	92.84	215.2
L^{III}	9.36	10.81	21.45	32.43	67.02	71.52	74.12	281.1
L^{IV}	19.79	24.18	26.95	29.88	77.32	90.24	90.39	212.5
L^V	12.98	20.43	23.38	27.21	31.61	38.21	84.69	373.6
Acarbose	2.90	9.44	13.02	16.18	81.23	97.15	97.72	240.6

Table 5 α-amylase inhibitory activity of ligands L^I–L^V and their IC_{50} value

Ligand	%Inhibition at each concentration (μM)							IC_{50} (μM)
	10	40	80	140	260	400	500	
L^I	12.9	14.9	18.1	27.7	31.8	42.4	45.4	501.93
L^{II}	9.7	12.1	12.9	15.2	26.7	29.7	32.6	772.2
L^{III}	9.1	9.5	11.0	12.0	16.8	26.0	28.9	984.4
L^{IV}	11.0	11.1	11.4	12.2	12.9	13.3	22.5	2416.0
L^V	12.2	13.0	13.3	17.8	18.8	20.4	23.7	1618
Acarbose	1.2	1.6	6.0	26.4	39.8	65.1	74.8	301.9

Fig. 1 Lineweaver–Burk plot for kinetic studies of α-glucosidase.

Fig. 1. This shift in both kinetic parameters and the line intersection pattern supports a mixed inhibition mechanism with uncompetitive characteristics, rather than a purely uncompetitive model, where the inhibitor likely binds both the free enzyme and the enzyme–substrate complex, with a higher affinity for allosteric sites.[47]

The Lineweaver–Burk plot for α-amylase indicates that the inhibitor increases V_{max} and K_m as shown in Fig. 2. These results indicate that the inhibitor likely acts *via* a mixed-type inhibition mechanism with a predominantly competitive component, as the increase in K_m suggests the inhibitor competes with the substrate for the enzyme's active site, while the increase in V_{max} may arise from minor conformational changes enhancing enzyme turnover under certain conditions.[48]

3.5. DNA binding studies

3.5.1. UV-visible spectroscopy

3.5.1.1. Spectrophotometric titrations of ligands with ct-DNA. UV-visible spectroscopy is a commonly used technique for studying the binding patterns of small compounds or medicines to DNA/proteins by measuring absorbance changes and wavelength shifts. When double-stranded DNA interacts with ligands, it normally exhibits one of two responses: hypochromicity or hyperchromicity.[49] A hypochromic reaction typically indicates an intercalative method of binding, whereas hyperchromicity is frequently related with electrostatic interactions or partial uncoiling of the DNA helix, which exposes more bases and shows significant binding of the molecule to ct-DNA. To investigate the interaction between pyrazole chalcone (L^I–L^V) absorption spectra were obtained at a fixed ligand concentration (50 μM) while gradually increasing the concentration of ct-DNA from 0 to 80 μM. For all ligands, a significant hypochromic effect with a modest bathochromic shift was seen
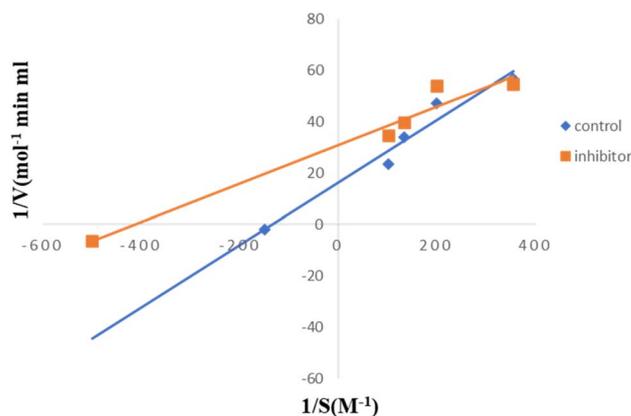
in the absorption bands as shown in Fig. 3. The observed hypochromicity suggests a significant contact between the aromatic chromophores π–π* transition bands and the DNA bases, which is a characteristic property of intercalative binding. Furthermore, the bathochromic shift reflects the stabilisation of the excited state of ligands upon complexation with DNA, supporting the intercalative binding strategy.[50]

To evaluate the binding affinities of the ligands, the intrinsic binding constant (K_b) was determined by monitoring changes in the absorbance of the ligands transfer bands upon incremental addition of ct-DNA. The value of K_b was obtained from a plot of $A_0/A − A_0$ *versus* 1/[DNA] (Fig. 4), using the relation:

$$\frac{A_0}{A - A_0} = \frac{\varepsilon_G}{\varepsilon_{(H-G)} - \varepsilon_G} + \frac{\varepsilon_G}{\varepsilon_{(H-G)}} \times \frac{1}{K[\text{DNA}]}$$

where, A_0 and A are the absorbance of the ligand in the absence and presence of the DNA respectively. ε_G and $\varepsilon_{(H-G)}$ are the absorption coefficients of drug and drug-DNA complex, respectively. The binding constant (K_b) is determined as the slope to intercept ratio. The size of K_b value indicates the extent of binding. Also, the Gibbs free energies are calculated from the relation:

$$\Delta G = -RT \ln(K_b)$$

All five ligands (L^I–L^V) bind to ct-DNA spontaneously with positive binding constants and negative standard Gibbs free energies. The equilibrium binding constants vary from 10^3–10^4 M^{-1}, with ΔG values of −16.6 to −23.9 kJ mol^{-1} (Table 7). These values are typical of non-covalent DNA interactions and are compatible with an intercalative binding mode inferred from UV-Vis titrations. Among the series L^I, L^{III} and L^V have the

Table 6 Kinetic parameters and mode of inhibition for α-glucosidase and α-amylase

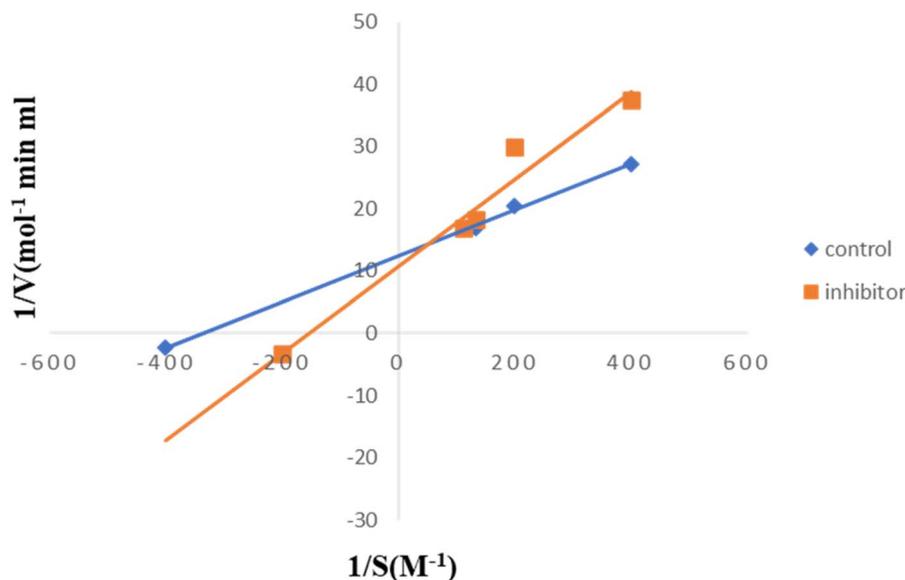| Enzyme	Concentration	V_{max}	K_m	Type of inhibition
α-glucosidase	Control	0.06079	0.007392	Mixed inhibition
	100 μM	0.03221	0.002412	
α-amylase	Control	0.08007	0.002962	Mixed inhibition
	50 μM	0.092618	0.0064925	

Fig. 2 Lineweaver–Burk plot for kinetic studies of α-amylase.

highest affinity for ct-DNA, suggesting optimal stacking and insertion between base pairs.[51]

3.5.1.2. Spectrophotometric titrations of Ct-DNA with ligands. The initial DNA spectrum showed a characteristic absorption at 260 nm (attributed to the π–π* electronic transitions of nucleobases) which underwent substantial modification with increasing compound concentration suggesting profound alterations in the DNA structure upon binding. UV-Vis absorption studies of ligands L^I–L^V revealed persistent hyperchromism with increasing concentration, indicating efficient interaction with the DNA double helix. The ligands L^I, L^{II}, and L^V showed significant bathochromic shifts, indicating changes in the electrical environment of DNA bases during binding. In contrast, ligands L^{III} and L^{IV} did not show substantial peak shifts, but merely intensity fluctuations, which are indicative of groove binding. The overall spectral behaviour, particularly the absence of strong hypochromism or large red shifts, rules out intercalative binding and favours a groove binding mode. The absorption plot are presented in Fig. S23. In this method, the ligands place themselves within the minor or major grooves of the DNA helix, interacting *via* hydrogen bonding, van der Waals forces, and electrostatic interactions to change base stacking without significantly distorting the helical structure. These observations suggest that the five ligands (L^I–L^V) primarily interact with DNA through groove binding.[52]

The plot of $1/(A - A_0)$ (where A_0 is the initial absorbance of free DNA at 260 nm and A is the absorbance of DNA in the presence of varied drug concentrations) *vs.* 1/[drug] shows a linear relationship. The binding constant can be calculated by dividing the intercept by the slope. The binding constants and Gibbs free energies calculated are presented in Table S1.[53]

3.5.2. Emission spectroscopy

3.5.2.1. Fluorescence quenching studies. To further investigate the interaction between ligands and DNA, we utilised well-established fluorescent dye binding mechanisms. Small molecules that compete with bound dyes in the DNA helix are likely to bind similarly. Adding a tiny molecule can alter the fluorescence intensity of the dye-DNA complex, providing valuable information on the interaction mode. EB is a very sensitive fluorescent probe that attaches to DNA by an intercalative mechanism. Due to fluorescence quenching by solvent molecules, EB does not emit significantly in an aqueous solution. The intercalation of EB within DNA base pairs increases its fluorescence intensity significantly. The property of EB is used in DNA binding research to assess the binding mode.[54] The fluorescence intensity decreased significantly after adding ligands to the EB-ct-DNA system as represented in Fig. 5. This behaviour strongly shows that all ligands actively compete with EB for binding sites inside the DNA helix. Ligands displacement of EB indicates that it primarily interacts with ct-DNA through an intercalative binding mechanism, stabilising the DNA-ligand complex *via* π–π stacking interactions. Fluorescence quenching measurements (Table 8) show that all ligands had moderate affinity for ct-DNA ($K_b \approx 10^2$–10^4 M^{-1}) and Stern–Volmer quenching constants in the order of 10^3 M^{-1}, indicating efficient quenching by static complex formation. The apparent binding site values ($n \approx 1$) for most ligands suggest about 1 : 1 stoichiometry, while L^{II} ($n = 1.19$) indicates the presence of additional or cooperative binding sites. The ligands L^{II} and L^{III} have the highest binding affinities, whereas L^V has the lowest. These findings combined with hypochromism and bathochromic changes seen in UV-Vis spectra demonstrate that the ligands interact with DNA in an intercalative manner with aromatic moieties inserting between base pairs resulting in fluorescence quenching and persistent ligand-DNA complex formation.

The data of fluorescence quenching is analysed using the Stern–Volmer equation:
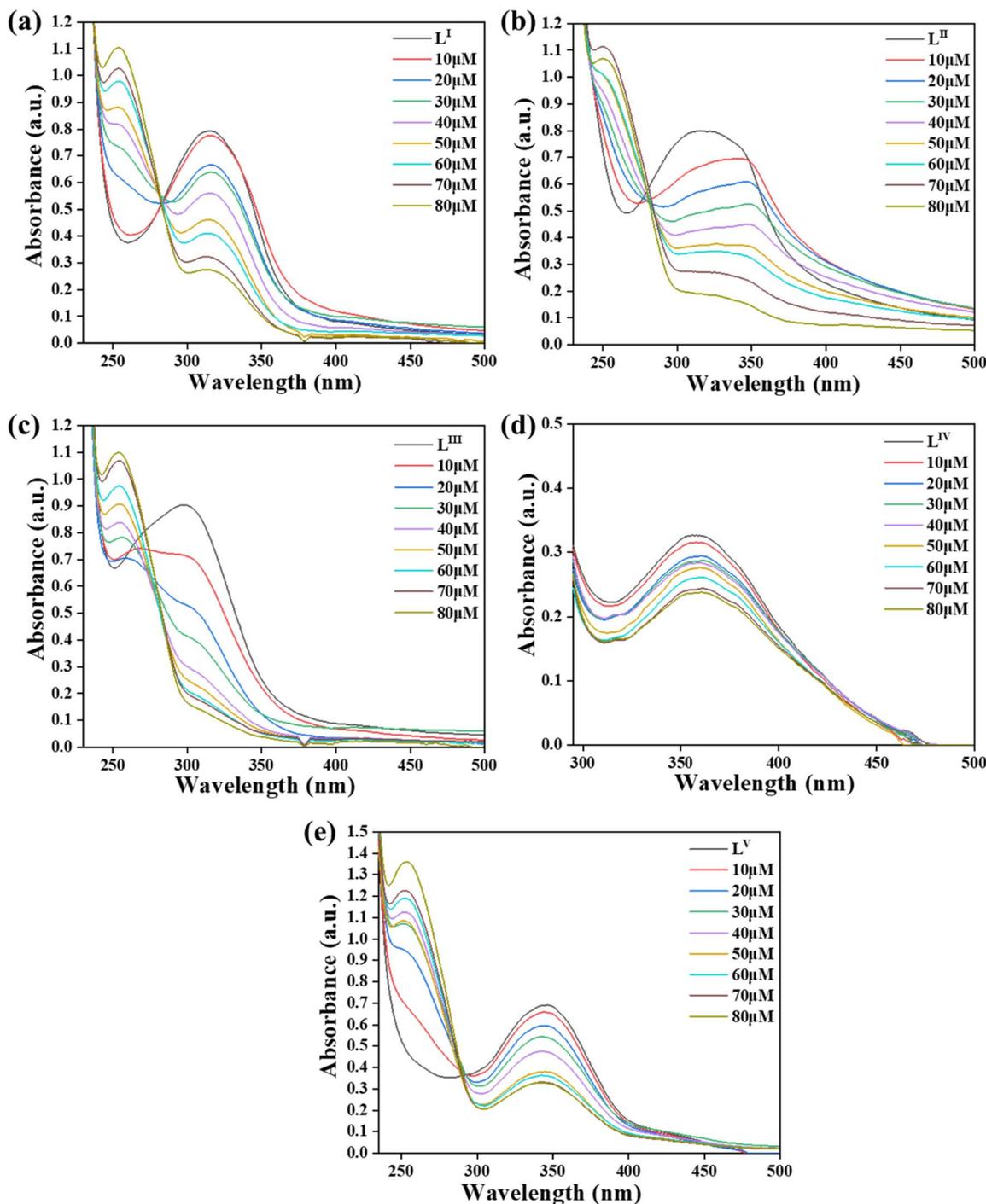
Fig. 3 UV-visible absorption spectra of the ligands (a) L^{I}, (b) L^{II}, (c) L^{III}, (d) L^{IV}, (e) L^{V}, with increasing concentrations of ct-DNA (0–80 μM).

$$\frac{F_0}{F} = 1 + K_{sv}[Q]$$

The fluorescence intensity of the molecule before and after adding the quencher is represented by F_0 and F, respectively. The quencher concentration is represented as [Q], while the Stern Volmer constant (K_{sv}) is determined from the slope of the linear plot of F_0/F *versus* [Q]. The K_{sv} values for the interaction of ct-DNA with ligands were found to be in the order of 10^3 M^{-1},

indicating a significant interaction between ct-DNA and ligands that results in fluorescence quenching. The binding constant (K_b) and binding stoichiometry (n) were determined using the modified Stern–Volmer equation given below:

$$\frac{\log(F_0 - F)}{F} = \log K + n \log[Q]$$

Here, K represents the binding constant, and n denotes the number of binding sites, which can be obtained from the intercept
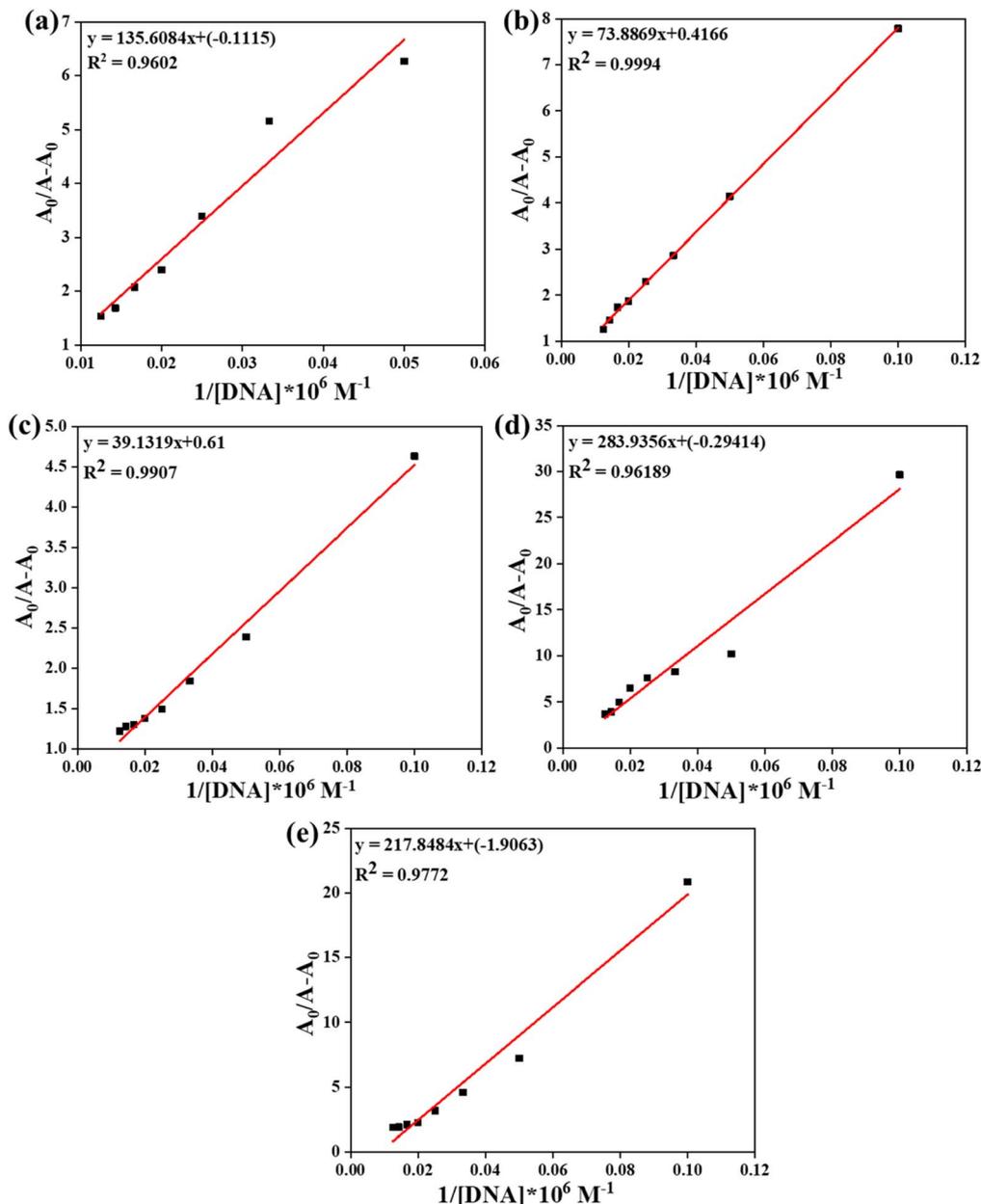
Fig. 4 Plot of $A_0/A - A_0$ vs. 1/[DNA] for ligands (a) L^I, (b) L^{II}, (c) L^{III}, (d) L^{IV}, (e) L^V.

Table 7 Binding modes and binding parameters for ligands (L^I–L^V)

Ligand	Interaction mode	Binding constant (k_b) (M^{-1})	ΔG (kJ mol^{-1})
L^I	Intercalative	8.22×10^2	-16.6
L^{II}	Intercalative	5.64×10^3	-21.4
L^{III}	Intercalative	15.59×10^3	-23.9
L^{IV}	Intercalative	1.04×10^3	-17.2
L^V	Intercalative	8.75×10^3	-22.5

and slope of the logarithmic regression plot of $\log[(F_0 - F)/F]$ versus $\log[Q]$, respectively[55] (Fig. 6). The calculated binding parameters from quenching studies are represented in Table 8.

3.5.2.2. Steady state fluorescence. The DNA-ligand binding interactions were investigated using fluorescence spectroscopy measurements in the wavelength range of 340–400 nm. The emission spectra displayed a characteristic peak at approximately 370–375 nm, with varying fluorescence intensities observed at different ligand concentrations while maintaining a constant DNA concentration. The systematic enhancement in fluorescence intensity for L^I, L^{II} with increasing ligand concentration (from 0 to 50) suggests strong binding interactions between the ligand and DNA. This hyperchromic effect, evidenced by the progressive increase in fluorescence intensity from the baseline to the maximum intensity indicates intercalative or groove binding modes of interaction between the L^I–
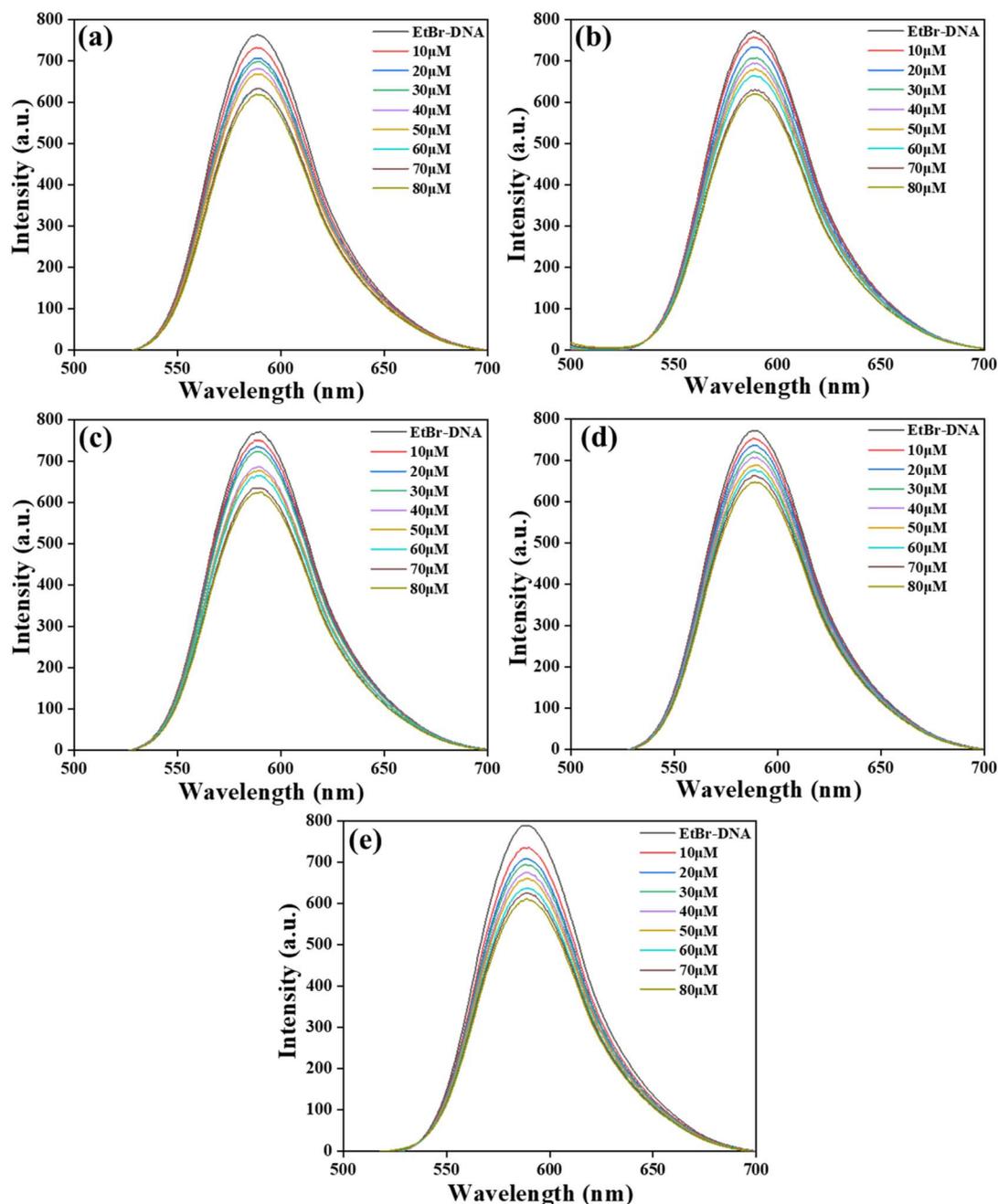
Fig. 5 Competitive displacement assays of dye ct-DNA with ligands (a) L^I, (b) L^{II}, (c) L^{III}, (d) L^{IV}, (e) L^V.

L^{II} and DNA as shown in Fig. 5. The fluorescence spectral profile of L^{III}–L^V remains unaltered and exhibits no detectable modifications or variations. No shifts in emission wavelengths, changes in peak intensities, or alterations in the overall spectral shape were observed during the analysis.[56] The emission spectra of these ligands are given in Fig. S25.

Table 8 Binding parameters and Stern–Volmer constants for the interaction of ligands with ct-DNA

Ligand	Quenching constant (K_{sv}) (M^{-1})	Binding constant (K_b) (M^{-1})	Binding sites (n)
L^I	2.77×10^3	5.068×10^2	0.81595
L^{II}	3.25×10^3	185.53×10^2	1.18625
L^{III}	3.03×10^3	43.158×10^2	1.04425
L^{IV}	2.39×10^3	12.83×10^2	0.93676
L^V	3.21×10^3	1.534×10^2	0.66539

3.5.3. Electrochemical studies. Cyclic voltammetry (CV) is extensively employed to assess the binding mode and interaction strength between drugs and DNA. Changes in peak potential and peak current of in the presence of compound/DNA indicate interaction between them. These variations can be utilized to determine the binding nature. In general, a shift in peak potential towards the positive direction suggests that the compound interact with DNA by intercalation. If the peak potential shifts in a negative direction, the compound interacts with DNA by minor/major groove binding or electrostatic binding. The cyclic voltammetry studies of ligands L^I–L^V in the

presence of increasing concentration of ct-DNA revealed distinct binding behaviours (shown in Fig. 7). For L^I, L^{II}, and L^V, a progressive decrease in peak current along with a negative shift in redox potential was observed, consistent with groove binding mode where the ligands interactions with the phosphate backbone rather than classical intercalation. In contrast, L^{III} and L^{IV} displayed current suppression accompanied by small positive or negligible potential shifts, suggesting an intercalation interaction where ligand insert between DNA base pairs, stabilizing the oxidized form and hindering electron transfer. These observations agree with the general
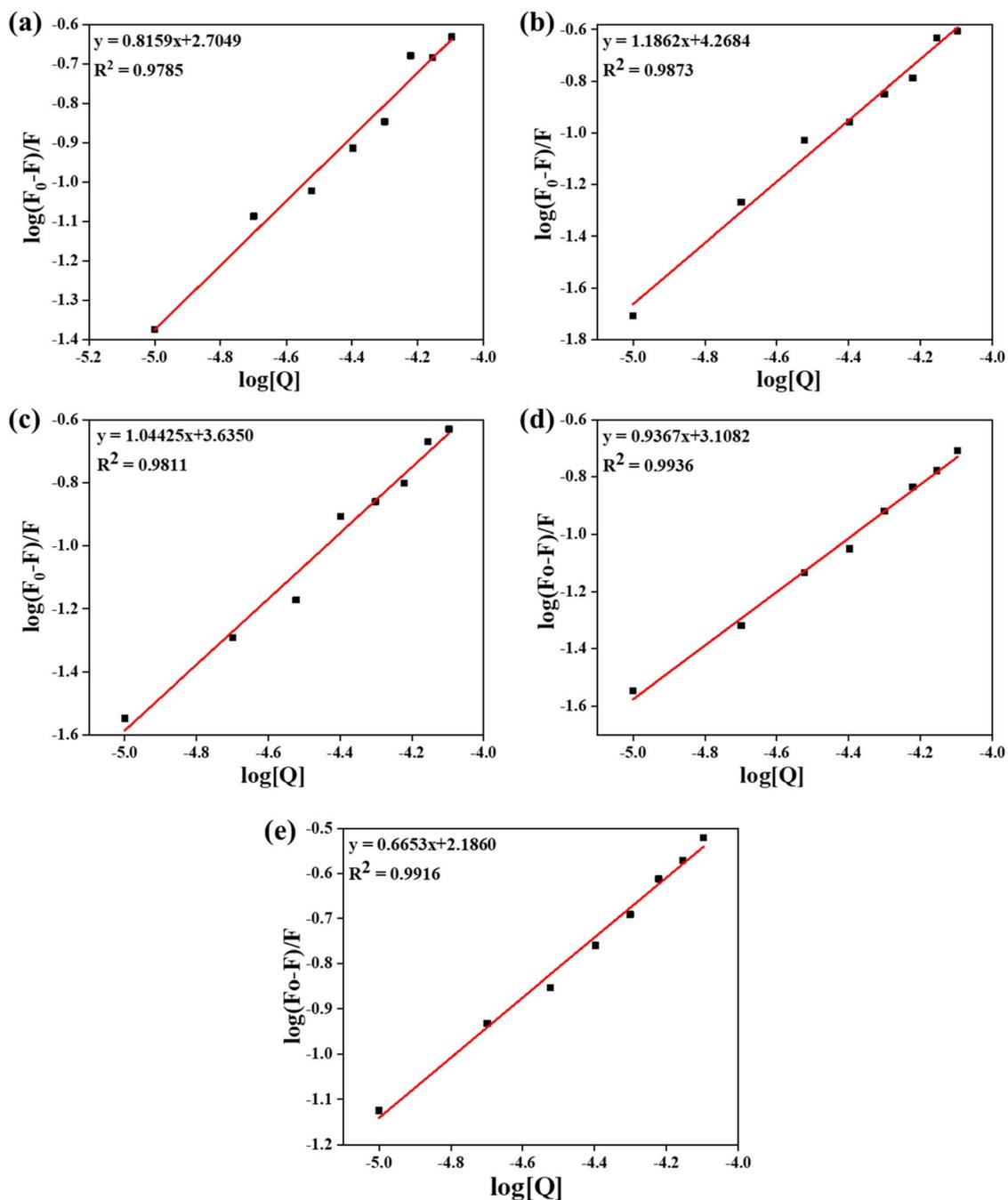

Fig. 6 Plot of log[Q] vs. log($F_0 - F$)/F for ligands (a) L^I, (b) L^{II}, (c) L^{III}, (d) L^{IV}, (e) L^V.

electrochemical signatures of DNA binding and highlight the structural influence of ligand frameworks on binding preference.[57]

Further as ligand concentration increased, the voltammograms exhibited a drop in peak current (I_p) and minor shifts in peak potential (E_p), indicating ligand-DNA interactions. The current suppression results from the production of DNA-ligand complexes with lower diffusion coefficients than the free ligand, indicating intercalative binding. The observed potential change confirms this, as binding modifies the redox microenvironment. The ligands' planar π-conjugated structure is anticipated to facilitate π–π stacking with DNA bases. Thus, the CV results (Fig. S26) indicate that ligands **L^I–L^V** bind DNA mostly through intercalation.[58]

3.6. Molecular docking studies

Docking is an *in silico* technique used to explore all possible interactions between a specific ligand (or group of ligands) and a target receptor (or group of receptors) using defined algorithms. It helps predict the binding affinity of a compound to a receptor by calculating the binding energy through computational models. When a compound is docked to a receptor various types of ligand–receptor interactions such as hydrogen bonding, hydrophobic interactions, van der Waals forces, and electrostatic interactions can be analysed.[59] The computational studies revealed that all compounds exhibited favourable binding energies ranging from −4.3 to −5.8 kcal mol^{-1} for α-amylase and from −4.6 to −6.1 kcal mol^{-1} for α-glucosidase, with consistent binding orientations within the protein
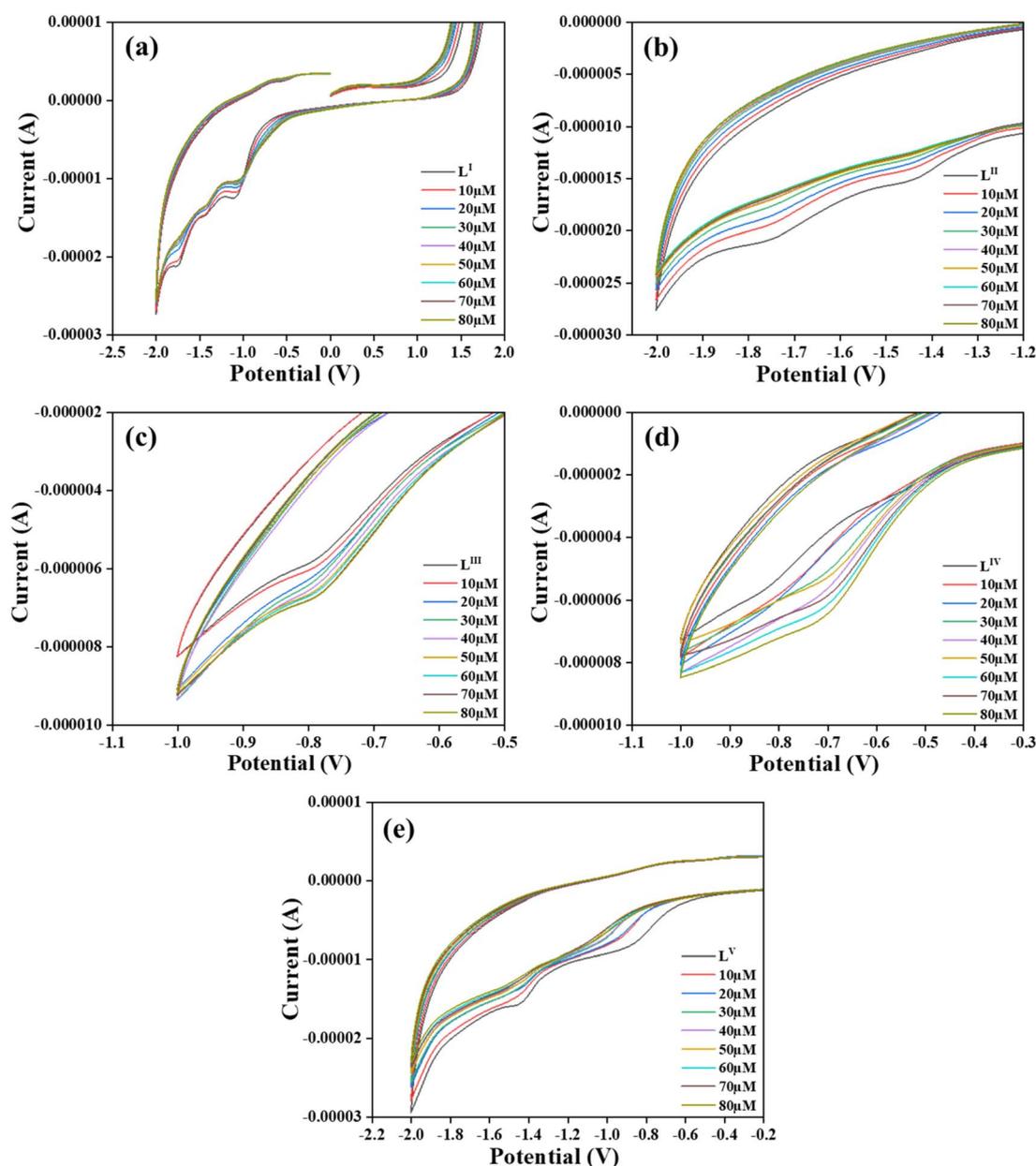

Fig. 7 Cyclic Voltammograms of ligands L^I–L^V (a–e) with increasing concentration of ct-DNA (10–80 μM).

structure. Among all derivatives, ligand L^{II}, exhibited the most energetically favourable interaction with a binding energy of −5.8 and −6.1 kcal mol^{-1} for α-amylase and α-glucosidase respectively and interacts through ALA-A480, LEU-A428, ILE-A477, ALA-A1, HIS-A108, VAL-A225 amino acid residues as shown in Fig. 8 and 9. Detailed analysis of the docking conformations revealed multiple stabilizing interactions between ligand L^{II} and amino acids of proteins, including hydrogen bonding networks, non-covalent interactions, and hydrophobic associations. The molecular visualization of the docked complexes confirmed the formation of stable protein-ligand complexes, with ligand L^{II} showing particularly strong molecular recognition features, suggesting its potential role in protein-targeted therapeutic applications. All other ligands exhibited higher (less negative) binding energies compared to L^{II}, indicating lower binding affinity. Hydrogen bonding in the ligands primarily involves the carbonyl oxygen, nitrogen atom, and hydroxyl groups. Additionally, hydrophobic interactions are facilitated by the presence of benzene rings, ethylene moieties, and methyl groups.[60] The binding energy value of ligands and hydrogen bonding is shown in Table 9 below. The binding interactions between ligands and target enzymes are illustrated in Fig. S27–S34.

3.7. Physicochemical properties

Physicochemical properties play a pivotal role in determining a molecule's efficacy, safety, and metabolic fate, and these can be predicted using established guidelines such as Lipinski's Rule of Five, Veber's rule, or Muegge's rule. In the present study, we applied Lipinski's criteria for assessing oral drug-likeness, which stipulate that a compound should possess ≤10 hydrogen bond acceptors (HBA), ≤5 hydrogen bond donors (HBD), a molecular weight below 500 Da, and a log P (octanol–water partition coefficient) not exceeding 5. Key

physicochemical properties include molecular weight, rotatable bonds (NRB), hydrogen bond acceptors (HBA), hydrogen bond donors (HBD), molar refractivity (MR), and polar surface area (PSA) are all calculated for respective ligands. In addition, lipophilicity and solubility are critical factors for successful drug development. The predicted physicochemical parameters of pyrazole chalcone derivatives, obtained using Swiss ADME are presented in Table 10. Examination of Table 10 indicates that all the evaluated compounds fully comply with Lipinski's Rule of Five, satisfying each of its parameters without exception. This compliance strongly suggests that the molecules possess favourable drug-likeness characteristics, with the potential for efficient absorption, optimal permeability, and satisfactory oral bioavailability. Hence, the investigated compounds demonstrate promising attributes for further development as orally active drug candidates.[61,62]

3.8. Prediction of ADMET properties

The enzyme inhibition studies indicated that all compounds exhibited similar biological activities. To further validate these designed molecules as potential drugs, we therefore evaluated their pharmacokinetic characteristics through ADMET analysis and drug-likeness assessment. ADMET properties were predicted *in silico* using the pkCSM online platform (Table 11), while drug-likeness characteristics were evaluated through the SwissADME online tool (Table 12). The results indicated excellent absorption potential, as all compounds achieved values greater than 90% for human intestinal absorption-significantly higher than the 30% cutoff that defines poor absorption. Volume of distribution (VDss) values exceeding 0.45 are considered indicative of high tissue distribution. Blood–brain barrier (BBB) and central nervous system (CNS) permeability were evaluated using established thresholds: log BB values of >−0.3 to <−1 and log PS values of >−2 to <−3, respectively.
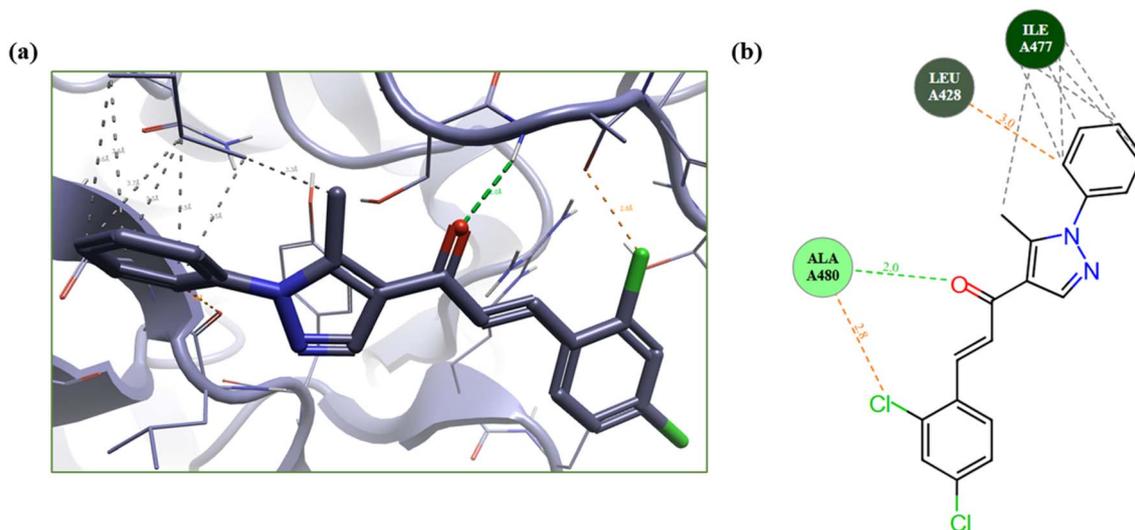

Fig. 8 (a) Molecular docking pose of L^{II} in catalytic site of α-glucosidase protein. (b) 2D interaction map highlighting the ligands bonding pattern with amino acid residues illustrating hydrogen-bond and hydrophobic interactions responsible for binding stability.

Fig. 9 (a) Molecular docking pose of L^{II} in catalytic site of α-amylase protein. (b) 2D interaction map highlighting the ligands bonding pattern with amino acid residues illustrating hydrogen-bond and hydrophobic interactions responsible for binding stability.
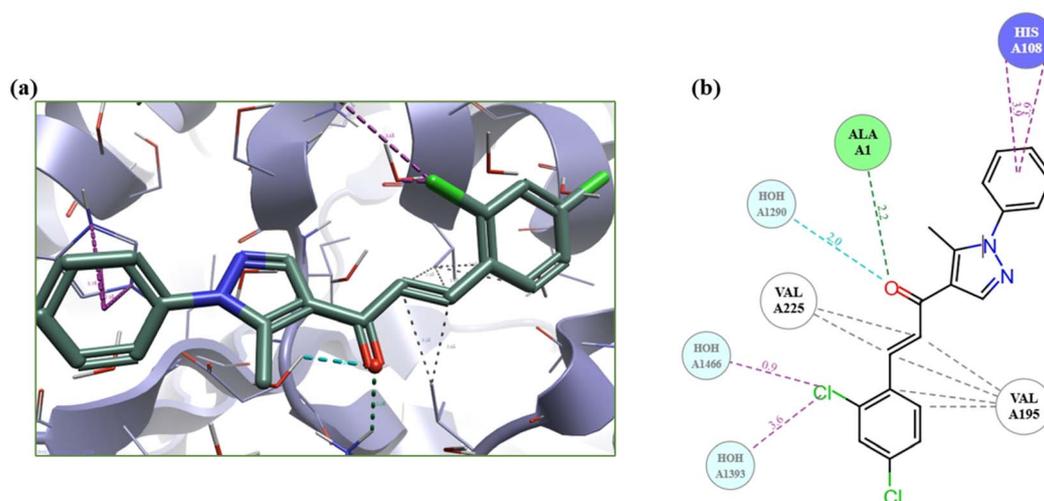
Compounds with log BB < −1 show poor brain distribution, while log BB > −0.3 indicates BBB crossing potential. Similarly, log PS > −2 suggests CNS penetration ability, whereas log PS < −3 indicates poor CNS entry. Based on these criteria ligands L^{I}, L^{II}, and L^{IV} show the most promising potential for crossing both BBB and CNS barriers, while L^{III} shows moderate barrier-crossing ability and L^{V} demonstrates good overall permeability with slightly lower CNS penetration potential. Drug metabolism involves the body's chemical biotransformation of pharmaceutical compounds resulting in various metabolites with distinct physicochemical and pharmacological characteristics. Understanding drug metabolism and potential drug–drug interactions is essential for drug development.

Cytochrome P450 (CYP450) serves as a crucial component in this process as this major hepatic enzyme system mediates phase 1 oxidative metabolism. Despite the existence of 17 CYP families in humans drug metabolism is limited to CYP1, CYP2, CYP3, and CYP4 families. Remarkably, just five isoforms (CYP1A2, CYP2C9, CYP2C19, CYP2D6, and CYP3A4) are responsible for metabolizing more than 90% of drugs undergoing phase I metabolism. From a metabolic perspective, all ligands are substrates for CYP3A4 but not CYP2D6, with L^{I}, L^{II}, L^{III}, and L^{V} showing similar moderate CYP inhibition profiles while L^{IV} presents the highest drug–drug interaction potential as it additionally inhibits CYP3A4 the same enzyme responsible for its own metabolism. Clearance represents

Table 9 Binding energies and hydrogen bonding interaction between ligands and proteins

Ligands	Binding energy (dG) (kcal mol^{-1}) (α-glucosidase)	Binding energy (dG) (kcal mol^{-1}) (α-amylase)	Hydrogen bonding (α-glucosidase)	Hydrogen bonding (α-amylase)
(L^{I})	−5.227	−4.470	N-ALA-A480	O-LYS-A101
(L^{II})	−6.153	−5.833	O-ALA-A480	O-ALA-A1
(L^{III})	−4.614	−4.336	N-ALA-A480	O-LYS-A101
(L^{IV})	−5.315	−4.719	N-ALA-A480	O-ALA-A1
(L^{V})	−5.558	−4.973	O-ALA-A480	O-ALA-A1
			OH-ASP-A423	OH-GLY-A192
Acarbose	−8.724	−7.297	O-ASP A423	O-ARG B12
			OH-THR A511	OH-GLU B50

Table 10 *In silico* physicochemical parameters predicted for pyrazole chalcone derivatives (L^{I}–L^{V})

Ligands	Formula	M.W.	HBD	HBA	Log P	NRB	PSA	MR	Log S	Violations
L^{I}	$C_{20}H_{18}N_2O$	302.37	0	2	3.97	4	34.89	93.30	−4.78	0
L^{II}	$C_{19}H_{14}Cl_2N_2O$	357.23	0	2	4.68	4	34.89	98.36	−5.67	0
L^{III}	$C_{19}H_{15}N_3O_3$	333.34	0	4	3.02	5	80.71	97.16	−4.53	0
L^{IV}	$C_{21}H_{17}N_3O$	327.38	1	2	2.26	4	50.68	100.19	−4.77	0
L^{V}	$C_{19}H_{16}N_2O_2$	304.34	1	3	3.22	4	55.12	90.36	−4.34	0

a pharmacokinetic parameter that relates drug concentration in the body to the rate of drug elimination. Lower total clearance values indicate prolonged drug retention in the body. Based on the clearance and toxicity analysis, ligand L^{II} demonstrated the most favourable drug persistence with the lowest clearance value, followed by L^V, while L^{IV} showed the highest elimination rate. Toxicity assessment using the AMES test revealed that L^I, L^{II}, and L^V exhibited non-toxic profiles, whereas L^{III} and L^{IV} showed potential mutagenic properties. Overall, L^{II} and L^V emerged as the most promising candidates, combining optimal drug persistence with favourable safety profiles for potential therapeutic development.[63]

Synthetic accessibility of the designed compounds was assessed using a scale ranging from 1 (easily synthesizable) to 10 (highly complex synthesis). All designed compounds achieved synthetic accessibility scores of approximately 3 (Table 12), indicating favourable synthetic feasibility. The ADMET analysis revealed that all ligands exhibited excellent intestinal absorption (>92%) and favourable pharmacokinetic profiles. Drug-likeness evaluation showed that all ligands satisfied all five drug-likeness rules. Overall, L^I and L^V emerged as the most promising candidates, combining excellent ADMET properties, complete drug-likeness compliance, and favourable safety profiles for potential therapeutic development.

3.9. Drug likeness and oral bioavailability

The bioavailability radar and boiled egg model, provided by the SwissADME web tool, are widely used graphical methods to predict drug-likeness and pharmacokinetic behavior of small molecules. The bioavailability radar evaluates six key physicochemical parameters-lipophilicity (LIPO), size, polarity, solubility (INSOLU), insaturation (INSATU), and flexibility (FLEX) with the optimal space for oral bioavailability represented by the pink region. Molecules falling largely within this zone are considered to have favorable oral drug-like properties. The Boiled Egg model, on the other hand, is based on lipophilicity (WLOGP) and polarity (TPSA) and predicts two important properties: passive human intestinal absorption (HIA, white zone) and blood–brain barrier (BBB) penetration (yellow zone). Additionally, it indicates whether compounds are substrates of P-glycoprotein (PGP), a key efflux transporter influencing drug distribution. Together, these plots provide a simple yet powerful visualization of absorption, distribution, and bioavailability characteristics, thereby aiding in the early selection of promising drug-like candidates.[64]

Analysis for ligands L^I–L^V provide an integrated overview of their drug-likeness and pharmacokinetic behaviour. The radar plots presented in Fig. 10 indicated that all ligands largely conformed to the optimal physicochemical space for oral bioavailability, with favourable lipophilicity, molecular size, polarity, solubility, and flexibility, while only slight deviations were observed in insaturation due to their aromatic nature, which may marginally affect solubility but does not compromise drug-likeness. The Boiled Egg analysis shown in Fig. 11 further complemented these findings positioning all ligands within the white region corresponding to high gastrointestinal absorption (HIA) while ligands such as L^I, L^{II}, and L^V were also located within the yellow zone, suggesting good blood–brain barrier (BBB) penetration and thus potential central nervous system activity. Importantly, most ligands were predicted as

Table 11 *In silico* ADMET parameters prediction of ligands L^I–L^V

Ligand	Absorption	Distribution			Metabolism							Excretion	Toxicity
					Substrate CYP		Inhibitor						
	Intestinal absorption (human)	VDss (human)	BBB	CNS	2D6	3A4	1A2	2C19	2C9	2D6	3A4	Total clearance	AMES toxicity
	Numeric (%absorbed)	Numeric (log LKg⁻¹)	Numeric (log BB)	Numeric (log PS)	Categorical (yes/no)							Numeric (log mL min⁻¹ kg⁻¹)	Categorical (yes/no)
L^I	95.008	0.246	0.612	−1.19	No	Yes	Yes	Yes	Yes	No	No	0.246	No
L^{II}	94.495	0.332	0.473	−1.258	No	Yes	Yes	Yes	Yes	No	No	0.152	No
L^{III}	94.807	0.076	−0.545	−2.032	No	Yes	Yes	Yes	Yes	No	No	0.263	Yes
L^{IV}	94.851	−0.145	0.43	−1.737	No	Yes	Yes	Yes	Yes	No	Yes	0.337	Yes
L^V	92.202	−0.024	0.373	−1.996	No	Yes	Yes	Yes	Yes	No	No	0.198	No

Table 12 Drug likeness prediction of ligands L^I–L^V based on lipnski, ghose, veber, egan, muegge and their synthetic accessibility

Ligand	Lipinski	Ghose	Veber	Egan	Muegge	Synthetic accessibility
L^I	Yes	Yes	Yes	Yes	Yes	2.77
L^{II}	Yes	Yes	Yes	Yes	No	2.79
L^{III}	Yes	Yes	Yes	Yes	Yes	2.89
L^{IV}	Yes	Yes	Yes	Yes	Yes	3.15
L^V	Yes	Yes	Yes	Yes	Yes	2.64

non-substrates of P-glycoprotein (PGP+), reducing the risk of efflux-mediated clearance and favouring enhanced tissue bioavailability, whereas a few displayed PGP+ tendencies which

may influence distribution. Collectively, these results highlight that ligands L^I-L^V exhibit strong oral absorption potential, good overall bioavailability, and, in some cases additional BBB
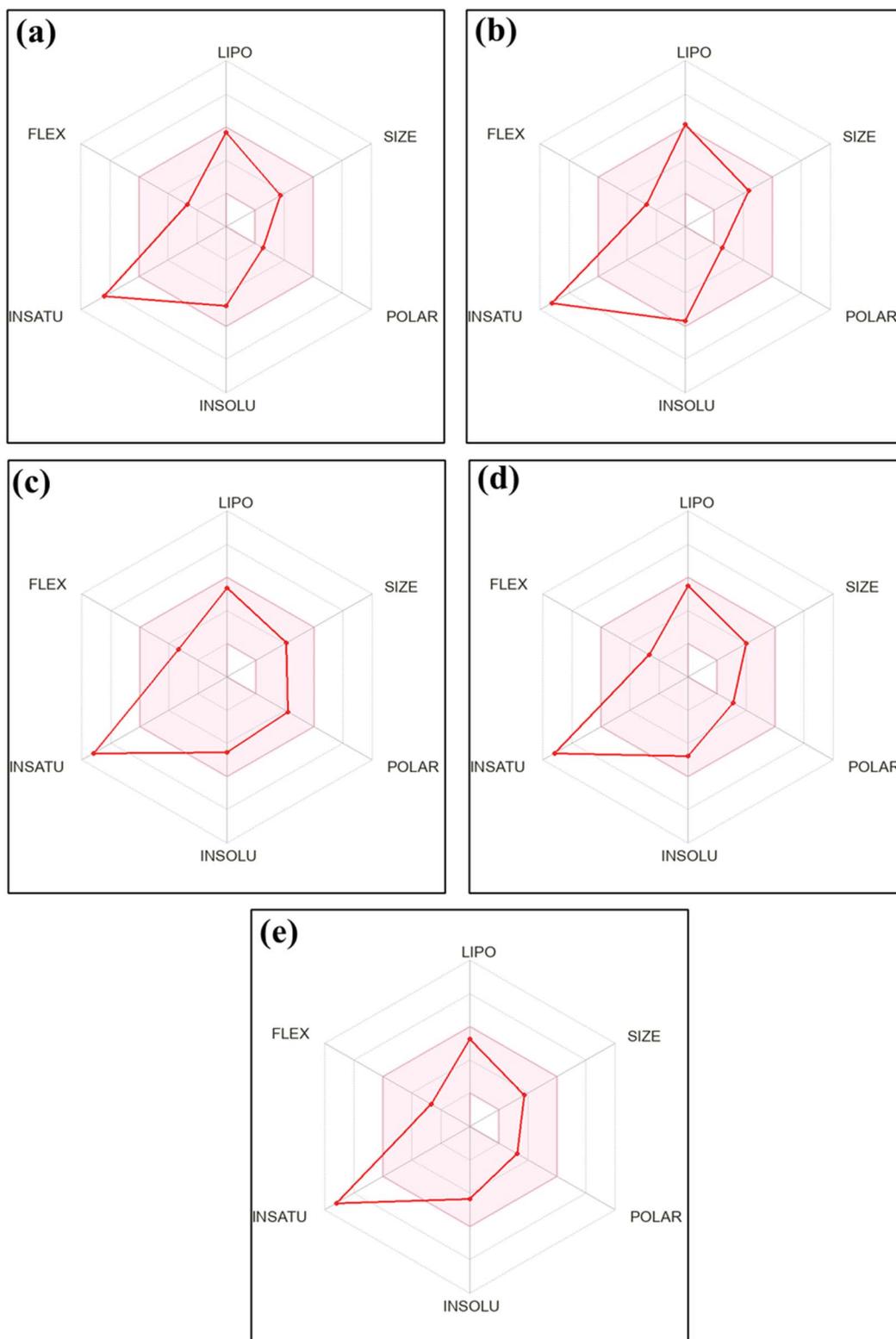

Fig. 10 Bioavailability radar plots of ligands; (a) L^I, (b) L^{II}, (c) L^{III}, (d) L^{IV}, (e) L^V, illustrating six key physicochemical parameters influencing oral drug-likeness: lipophilicity (LIPO), size (SIZE), polarity (POLAR), solubility (INSOLU), satura3ion (INSATU), and flexibility (FLEX). The pink zone represents the optimal range for drug-likeness; compounds with red traces enclosed within this area are predicted to possess favourable oral bioavailability.

permeability, underscoring their promise as drug-like scaffolds with potential applications in both peripheral and central therapeutic targets.

3.10. Density functional theory studies

The HOMO–LUMO energy gap (ΔE) is a fundamental descriptor of a molecule's electronic properties, reflecting its intramolecular charge transfer capacity and electrical conductivity. A smaller ΔE denotes higher polarizability, greater chemical reactivity and lower kinetic stability classifying the molecule as 'soft'. Conversely, a larger ΔE indicates a 'hard' molecule with greater stability and lower reactivity. According to Koopmans' theorem, the HOMO energy approximates the ionization potential (I), while the LUMO energy corresponds to the electron affinity (A). A larger ΔE typically implies increased resistance to redox processes and reduced chemical reactivity, often associated with aromatic stability. Furthermore, the electronic chemical potential (μ), indicative of the system's electron escape tendency, can be derived from ionization potential and electron affinity values. The calculated parameters[65] are summarised in Table 13.

The reaction kinetics can be analyzed by exploring the nature of HOMO and LUMO orbitals in terms of their hardness and softness. The ligand $\mathbf{L^{III}}$ exhibits the highest E_{HOMO}, indicating the softest HOMO and, consequently, the lowest ionization potential. Simultaneously, it has the highest E_{LUMO}, reflecting the hardest LUMO and thus the lowest electron affinity. A large energy gap between the HOMO and LUMO indicates greater resistance to both oxidation and reduction, reflecting low overall chemical reactivity a key feature commonly associated with aromatic stability. The global hardness (η) of the pyrazole chalcone series follows the same order as their HOMO–LUMO energy gap: $\mathbf{L^I} > \mathbf{L^{II}} > \mathbf{L^{III}} \approx \mathbf{L^V} > \mathbf{L^{IV}}$. This indicates that the compound $\mathbf{L^{IV}}$, despite having the lowest thermodynamic stability in the series, exhibits the highest global hardness. It is the least reactive toward oxidation and reduction processes, making it the hardest compound in the series. Its high hardness is primarily associated with its E_{LUMO} value. The Mulliken electronegativity (χ) trend in the series shows that the $\mathbf{L^{IV}}$ has the highest tendency to attract electrons, consistent with its soft LUMO and high electron affinity. In contrast, the $\mathbf{L^{III}}$ exhibits the lowest electron affinity due to its hard LUMO. However, the

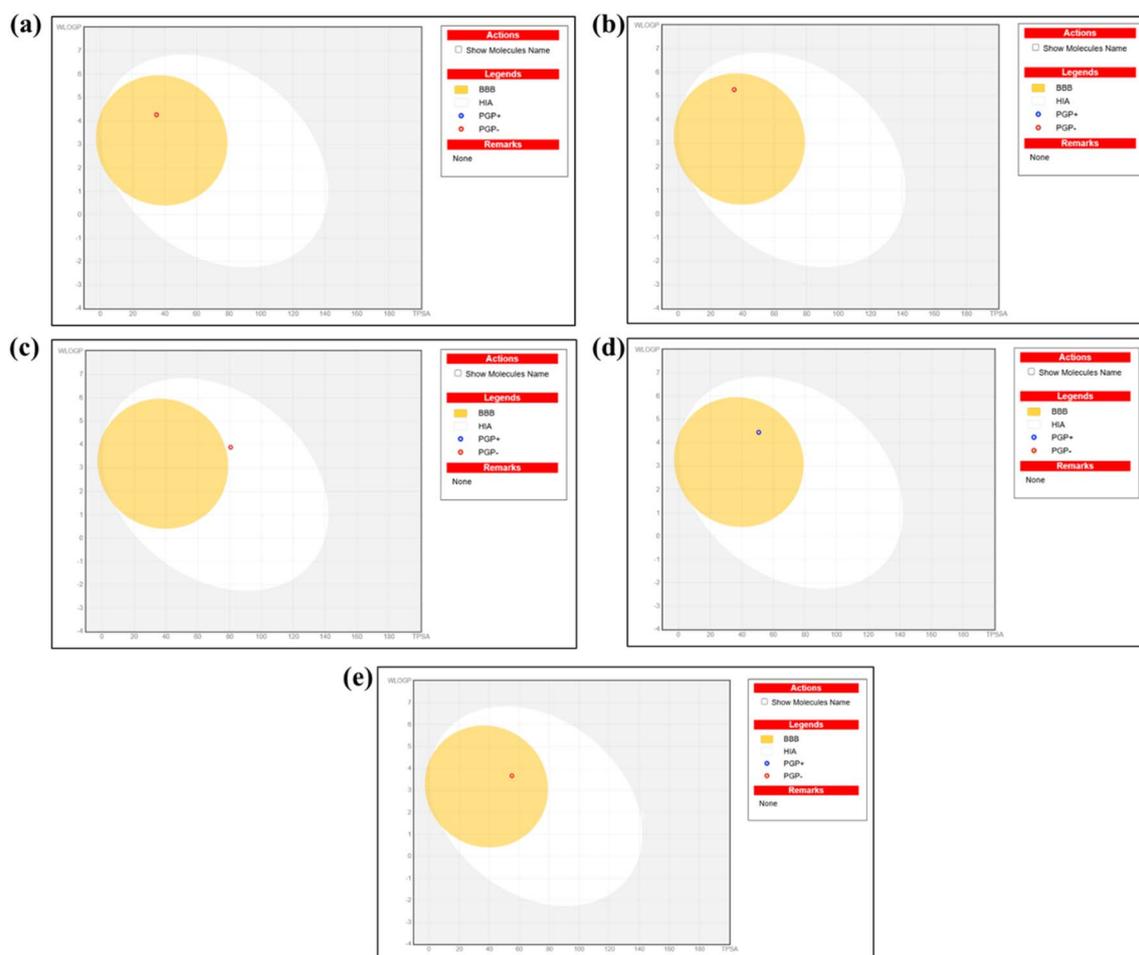**Fig. 11** BOILED-Egg model prediction of gastrointestinal absorption (GI) and blood–brain barrier (BBB) permeability for ligands; (a) L^I, (b) L^{II}, (c) L^{III}, (d) L^{IV}, (e) L^V. The yellow region represents high probability of passive GI absorption, while the white region indicates likelihood of brain penetration. Red and blue dots represent P-glycoprotein (P-gp) substrates and non-substrates, respectively.

**Table 13** Calculated DFT parameters of ligands L^I–L^V

Ligand	Energy gap (ΔE)	Chemical hardness (η)	Chemical potential (μ)	Electrophilicity index (ω)	Softness (S)	Absolute electronegativity (χ)
(L^I)	4.30	2.145	−4.055	3.832	0.466	4.055
(L^{II})	4.19	2.095	−4.345	4.505	0.477	4.345
(L^{III})	4.08	2.030	−3.650	3.281	0.492	3.65
(L^{IV})	3.93	1.965	−4.585	5.349	0.508	4.585
(L^V)	4.07	2.035	−3.835	3.613	0.491	3.835

trend of electronic chemical potential (μ) is inversely related to Mulliken electronegativity. Therefore, the L^{III} shows the greatest tendency to donate electrons, which can be linked to its highest chemical potential and its softest HOMO.[66]

The electrophilicity index (ω) of the chalcones series represent the combined effect of their electronic chemical potential and global hardness. The electrophilicity indices of the ligand series correspond to the trend observed in the absolute values of their electronic chemical potentials. Therefore, the ligand L^{III} exhibits the lowest electrophilicity index, indicating its minimal

tendency to accept additional electronic charge, consistent with its hard LUMO. In contrast, the ligand L^{IV} shows the highest ω value, reflecting its relatively softer LUMO and greater ability to accommodate electrons among the series.[67]

The HOMO and LUMO orbital surfaces of pyrazole chalcones were also calculated and are presented in Fig. 12. Fig. 12 shows that the HOMO orbitals of the compounds are primarily distributed over the pyrazole ring, the vinyl double bond, carbonyl group and the electron donating groups of phenyl ring. Conversely, the LUMO orbitals are delocalized across the entire
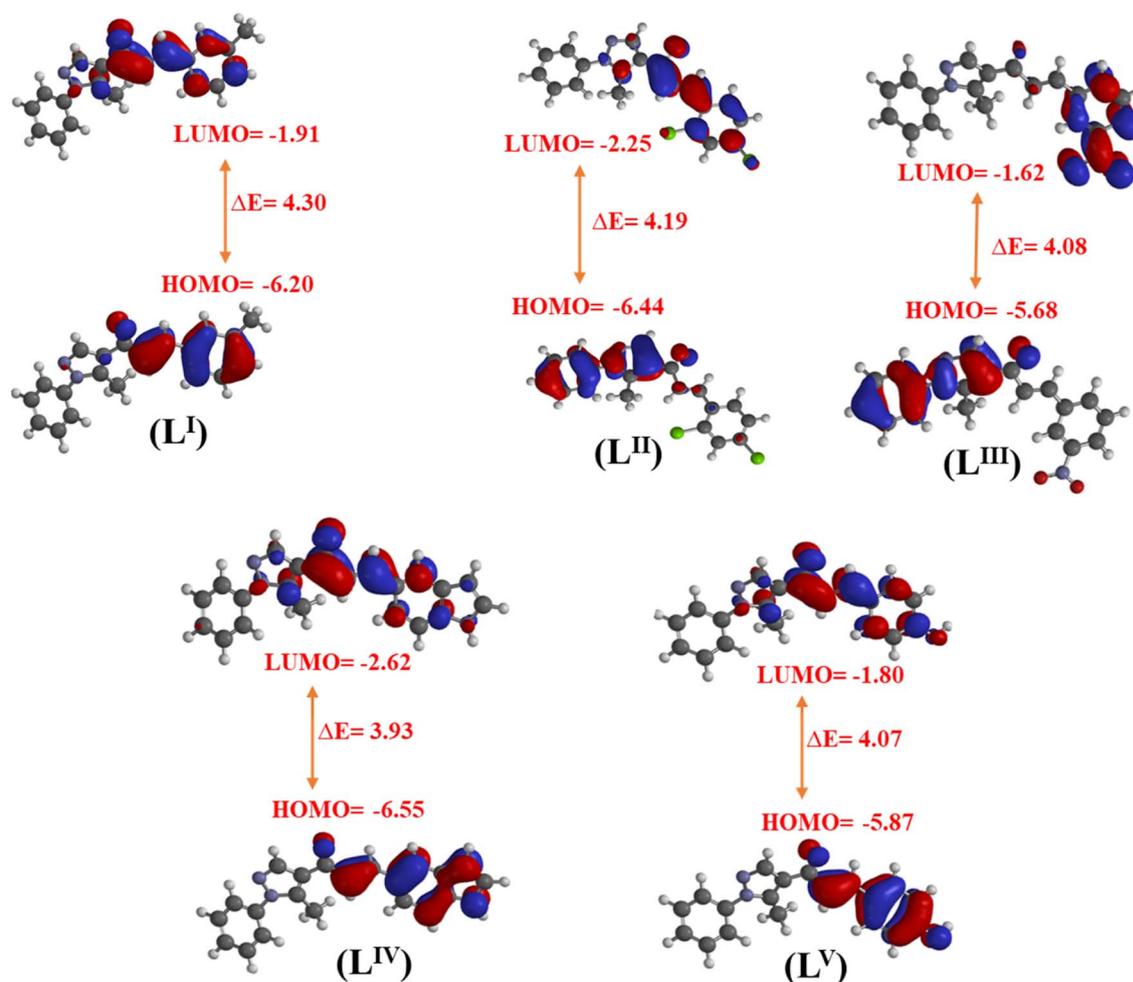
Fig. 12 Frontier molecular orbitals representation of ligands (L^I–L^V).

molecule, encompassing the pyrazole ring, ethylene double bond, carbonyl group, and the electron withdrawing groups of phenyl ring.

4. Conclusion

This study successfully demonstrates the potential of novel pyrazole-chalcone hybrids as dual α-amylase and α-glucosidase inhibitors for type 2 diabetes management. The microwave assisted synthesis methodology achieved remarkable efficiency reducing reaction times from 24 hours to 3–35 minutes while improving yields (approx. 80–85%) and product purity compared to conventional methods. Among the synthesized compounds L^{IV} exhibited superior α-glucosidase inhibition (IC_{50} = 212 μM) exceeding the standard drug acarbose (IC_{50} = 240.6 μM) while L^{I} demonstrated the strongest α-amylase inhibitory activity (IC_{50} = 501.9 μM). Kinetic analysis revealed mixed-type inhibition mechanisms for both enzymes suggesting multiple binding sites and potentially sustained therapeutic effects. Molecular docking studies confirmed favourable binding energies (-4.3 to -6.1 kcal mol^{-1}) with compound L^{II} showing optimal interactions with both target enzymes. DFT calculations provided insights into electronic properties with HOMO–LUMO gaps (3.93–4.30 eV) indicating suitable chemical stability. DNA binding studies revealed intercalative interactions for all ligands with binding constants of 10^{3}–10^{4}M^{-1}. The structure–activity relationships indicate that electron-withdrawing substituents and extended conjugated systems enhance enzyme binding affinity. ADMET and drug-likeness predictions indicated high intestinal absorption, good permeability, favourable metabolic stability, and acceptable safety profiles, particularly for L^{II} and L^{V}, making them strong candidates for further development. Collectively, these findings position pyrazole–chalcone hybrids as promising multifunctional scaffolds for next-generation antidiabetic therapeutics with potential advantages in efficacy, safety, and drug-likeness over existing agents.

Conflicts of interest

There is no conflict of interest mentioned by the authors.

Data availability

^{I}-L^{V}), Fig.S7-S12 (^{1}HNMR ^{I}-L^{V}), Fig.S13-S16 (^{13}C-NMR spectra of ligands L^{I}-L^{V}), Fig.S17-S22 (Mass spectra of ^{I}-L^{V}), Fig.S23-S24 (UV plots of DNA titrations) Fig.S25 (Emis^{I}-L^{V} with α-glucosidase and α-

All experimental data and analytical results are presented in the main text and supplementary information (SI) figures. Supplementary information: Table S1 (literature survey), Fig. S1–S6 (FTIR spectra of ligands L^{I}–L^{V}), Fig. S7–S12 (^{1}HNMR spectra of ligands L^{I}–L^{V}), Fig. S13–S16 (^{13}C-NMR spectra of ligands L^{I}–L^{V}), Fig. S17–S22 (mass spectra of ligands L^{I}–L^{V}), Fig. S23 and S24 (UV plots of DNA titrations), Fig. S25 (emission spectra of DNA titrations), Fig. S26 (cyclic voltammogram of DNA titrations), Fig. S27–S34 (docking interaction images of

ligands L^{I}–L^{V} with α-glucosidase and α-amylase proteins). See DOI: https://doi.org/10.1039/d5ra07397a.

Acknowledgements

References

1 X. Lin, Y. Xu, X. Pan, J. Xu, Y. Ding, X. Sun, X. Song, Y. Ren and P.-F. Shan, *Sci. Rep.*, 2020, **10**, 14790.

2 A. A. Motala, J. C. Mbanya, K. Ramaiya, F. J. Pirie and K. Ekoru, *Nat. Rev. Endocrinol.*, 2022, **18**, 219–229.

3 S. Matoori, *ACS Pharmacol. Transl. Sci.*, 2022, **5**, 513–515.

4 B. Gieroba, A. Kryska and A. Sroka-Bartnicka, *Biochem. Biophys. Rep.*, 2025, **42**, 102037.

5 R. Pop-Busui, J. L. Januzzi, D. Bruemmer, S. Butalia, J. B. Green, W. B. Horton, C. Knight, M. Levi, N. Rasouli and C. R. Richardson, *Diabetes Care*, 2022, **45**, 1670–1690.

6 S. Zheng, K. Huang and T. Tong, *J. Agric. Food Chem.*, 2021, **69**, 6145–6155.

7 N. W. X. Ong, B. Sim, J. J. Chang, J. H. M. Wong, X. J. Loh and R. Goh, *RSC Appl. Polym.*, 2023, **1**, 204–228.

8 E. L. Feldman, B. C. Callaghan, R. Pop-Busui, D. W. Zochodne, D. E. Wright, D. L. Bennett, V. Bril, J. W. Russell and V. Viswanathan, *Nat. Rev. Dis. Primers*, 2019, **5**, 41.

9 Y. Yao, X. Lei, Y. Wang, G. Zhang, H. Huang, Y. Zhao, S. Shi, Y. Gao, X. Cai, S. Gao and Y. Lin, *ACS Nano*, 2023, **17**, 22334–22354.

10 A. Gupta, T. Behl, A. Sehgal, S. Bhardwaj, S. Singh, N. Sharma and A. Hafeez, *Mol. Biol. Rep.*, 2021, **48**, 2863–2879.

11 R. P. Kshirsagar, A. A. Kulkarni, R. S. Chouthe, S. K. Pathan, H. D. Une, G. B. Reddy, P. V. Diwan, S. A. Ansari and J. N. Sangshetti, *RSC Adv.*, 2020, **10**, 1733–1756.

12 A. Rammohan, B. V. Bhaskar, N. Venkateswarlu, W. Gu and G. V. Zyryanov, *Bioorg. Chem.*, 2020, **95**, 103527.

13 M. Sohrabi, M. R. Binaeizadeh, A. Iraji, B. Larijani, M. Saeedi and M. Mahdavi, *RSC Adv.*, 2022, **12**, 12011–12052.

14 A. H.-M. Lin, B.-H. Lee and W.-J. Chang, *Food Hydrocolloids*, 2016, **53**, 163–171.

15 F. J. Warren, B. Zhang, G. Waltzer, M. J. Gidley and S. Dhital, *Carbohydr. Polym.*, 2015, **117**, 192–200.

16 A. Bhatnagar and A. Mishra, in *Natural Products as Enzyme Inhibitors*, ed. V. L. Maheshwari and R. H. Patil, Springer Nature Singapore, Singapore, 2022, pp. 269–283.

17 R. Mwakalukwa, Y. Amen, M. Nagata and K. Shimizu, *ACS Omega*, 2020, **5**, 20070–20079.

18 M. J. Van Der Maarel, B. Van der Veen, J. C. Uitdehaag, H. Leemhuis and L. Dijkhuizen, *J. Biotechnol.*, 2002, **94**, 137–155.

19 Y. Chinthala, S. Thakur, S. Tirunagari, S. Chinde, A. K. Domatti, N. K. Arigari, S. KVNS, S. Alam, K. K. Jonnala and F. Khan, *Eur. J. Med. Chem.*, 2015, **93**, 564–573.

20 S. Welday Kahssay, G. S. Hailu and K. Taye Desta, *Drug Des. Dev. Ther.*, 2021, **15**, 3119–3129.

21 H. Zhai, S. Zhang, M. Ampomah-Wireko, H. Wang, Y. Cao, P. Yang, Y. Yang, F. O. A. Frejat, L. Wang, B. Zhao, C. Ren and C. Wu, *Russ. J. Bioorg. Chem.*, 2022, **48**, 1175–1189.

22 U. Farwa and M. A. Raza, *RSC Adv.*, 2022, **12**, 22951–22973.

23 N. Bansal, E. Sathish, M. A. Babu, G. Bushi, A. M. Gaidhane, T. G. Singh, D. Singh, G. Alasiri, M. Fareed and B. Kumar, *Mol. Divers.*, 2025, 1–24.

24 R. Khator and V. Monga, *Future Med. Chem.*, 2024, **16**, 173–195.

25 A. M. Naglah, A. A. Almehizia, A. S. Al-Wasidi, A. S. Alharbi, M. H. Alqarni, A. S. Hassan and W. M. Aboulthana, *Pharmaceuticals*, 2024, **17**, 655.

26 S. Mortada, K. Karrouchi, E. H. Hamza, A. Oulmidi, M. A. Bhat, H. Mamad, Y. Aalilou, S. Radi, M. Ansar and A. Masrar, *Sci. Rep.*, 2024, **14**, 1312.

27 G. Li, Y. Cheng, C. Han, C. Song, N. Huang and Y. Du, *RSC Med. Chem.*, 2022, **13**, 1300–1321.

28 P. De Sena Murteira Pinheiro, L. S. Franco, T. L. Montagnoli and C. A. M. Fraga, *Expet Opin. Drug Discov.*, 2024, **19**, 451–470.

29 J. Sharma and R. Kaushal, *Russ. J. Gen. Chem.*, 2024, **94**, 1794–1814.

30 Q. Hu, Y. He, F. Wang, J. Wu, Z. Ci, L. Chen, R. Xu, M. Yang, J. Lin, L. Han and D. Zhang, *Chin. Med.*, 2021, **16**, 87.

31 G. Tiwari, A. Khanna, V. K. Mishra and R. Sagar, *RSC Adv.*, 2023, **13**, 32858–32892.

32 Y. Baqi and A. H. Ismail, *ACS Omega*, 2025, **10**, 7317–7326.

33 M. I. Farrim, A. Gomes, D. Milenkovic and R. Menezes, *Hum. Genomics*, 2024, **18**, 16.

34 N. Nadiger, J. K. Veed, P. Chinya Nataraj and A. Mukhopadhyay, *Clin. Epigenet.*, 2024, **16**, 67.

35 Y. Li, B. Sun, J. Zhai, L. Fu, S. Zhang, J. Zhang, H. Liu, W. Xie, H. Deng and Z. Chen, *Tetrahedron Lett.*, 2019, **60**, 151165.

36 M. M. Al-Kaabi, H. A. Al-Hazam, L. Al-Maliki, N. A. Al-Masoudi, B. A. Saeed, A. Shtaiwi and Y. A. Al-Soud, *J. Mol. Struct.*, 2025, **1321**, 139992.

37 M. Kaur and R. Kaushal, *J. Mol. Struct.*, 2023, **1271**, 133994.

38 M. Irfan Dar, M. I. Qureshi, S. Zahiruddin, S. Abass, B. Jan, A. Sultan and S. Ahmad, *ACS Omega*, 2022, **7**, 46156–46173.

39 R. Zhang, Y. Zhang, G. Huang, X. Xin, L. Tang, H. Li, K. S. Lee, B. R. Jin and Z. Gui, *RSC Adv.*, 2021, **11**, 38703–38711.

40 M. Freitas, C. Proença, D. Ribeiro, M. B. Quinaz-Garcia, A. N. Araújo and E. Fernandes, *J. Chem. Educ.*, 2023, **100**, 1237–1245.

41 H. A. A. Abd Al Hussain and D. N. M. Aljamali, *J. Pharm. Res. Int.*, 2021, **13**, 4234–4242.

42 H. V. Chavan, L. K. Adsul, A. S. Kotmale, V. D. Dhakane, V. N. Thakare and B. P. Bandgar, *J. Enzyme Inhib. Med. Chem.*, 2015, **30**, 22–31.

43 A. Urbonavičius, G. Fortunato, E. Ambrazaitytė, E. Plytninkienė, A. Bieliauskas, V. Milišiūnaitė, R. Luisi, E. Arbačiauskienė, S. Krikštolaitytė and A. Šačkus, *Molecules*, 2022, **27**, 3752.

44 P. Rai, P. Chettri, S. Kar, M. A. Nagar, S. Srivastava and N. R. Golakoti, *Chem. Pap.*, 2021, **75**, 2603–2615.

45 T.-H.-T. Phan, K. Hengphasatporn, Y. Shigeta, W. Xie, P. Maitarad, T. Rungrotmongkol and W. Chavasiri, *ACS Omega*, 2023, **8**, 26340–26350.

46 M. Kaur and R. Kaushal, *Appl. Organomet. Chem.*, 2021, **35**, e6042.

47 M. J. Mphahlele, M. M. Maluleka, Y. S. Choong, B. A. Monchusi and V. G. Mbazima, *Med. Chem. Res.*, 2022, **31**, 2243–2259.

48 S. Moein, M. Moein and H. Javid, *Evid. base Compl. Alternative Med.*, 2022, **2022**, 1–6.

49 F. S. Aljohani, A. M. Abu-Dief, R. M. El-Khatib, H. A. Al-Abdulkarim, A. Alharbi, A. Mahran, M. E. Khalifa and N. M. El-Metwaly, *J. Mol. Struct.*, 2021, **1246**, 131139.

50 A. A. Shanty and P. V. Mohanan, *Inorg. Nano-Met. Chem.*, 2023, **53**, 1380–1395.

51 A. A. Shanty and P. V. Mohanan, *Inorg. Nano-Met. Chem.*, 2023, **53**, 1380–1395.

52 M. Sirajuddin, S. Ali and A. Badshah, *J. Photochem. Photobiol., B*, 2013, **124**, 1–19.

53 N. Shahabadi, M. Falsafi and M. Maghsudi, *Nucleosides, Nucleotides Nucleic Acids*, 2017, **36**, 49–65.

54 M. F. Alam, S. Varshney, M. A. Khan, A. A. Laskar and H. Younus, *Int. J. Biol. Macromol.*, 2018, **113**, 300–308.

55 E. Oguzcan, Z. Koksal, T. Taskin-Tok, A. Uzgoren-Baran and N. Akbay, *Spectrochim. Acta Mol. Biomol. Spectrosc.*, 2022, **270**, 120787.

56 L. Jin, Y. Gao, Z. Sun, Y. Jia, B. Shen, X. Li, Q. Geng and X. Mu, *Polycyclic Aromat. Compd.*, 2023, **43**, 7252–7265.

57 S. Ponkarpagam, G. Mahalakshmi, K. N. Vennila and K. P. Elango, *Spectrochim. Acta Mol. Biomol. Spectrosc.*, 2020, **234**, 118268.

58 S. Ponkarpagam, G. Mahalakshmi, K. N. Vennila and K. P. Elango, *Spectrochim. Acta Mol. Biomol. Spectrosc.*, 2020, **234**, 118268.

59 J. Syahri, R. Hilma, A. H. Ali, N. Ismail, N. Y. Ling, B. A. Nurohmah, H. K. Agustar, L. Y. Ling and J. Latip, *RSC Adv.*, 2023, **13**, 36035–36047.

60 M. S. Islam, A. M. Al-Majid, E. N. Sholkamy, S. Yousuf, M. Ayaz, A. Nawaz, A. Wadood, A. U. Rehman, V. P. Verma and A. Bari, *J. Mol. Struct.*, 2022, **1269**, 133843.

61 J. G. M. Mvondo, A. Matondo, D. T. Mawete, S.-M. N. Bambi, B. M. Mbala and P. O. Lohohola, *Int. J. Trop. Dis. Health*, 2021, **42**, 1–12.

62 M. T. Mahanthesh, D. Ranjith, R. Yaligar, R. Jyothi, G. Narappa and M. Ravi, *J. Pharmacogn. Phytochem.*, 2020, **9**, 1799–1809.

63 H. Hadni and M. Elhallaoui, *New J. Chem.*, 2020, **44**, 6553–6565.

64 A. Daina, O. Michielin and V. Zoete, *Sci. Rep.*, 2017, **7**, 42717.

65 H. Karaca and S. Kazancı, *J. Mol. Struct.*, 2022, **1248**, 131454.

66 H. A. Hussein and G. F. Fadhil, *ACS Omega*, 2023, **8**, 4937–4953.

67 H. A. Hussein and G. F. Fadhil, *ACS Omega*, 2023, **8**, 4937–4953.